

Self-Calibration for the LOFAR Radio Astronomical Array

Sebastiaan van der Tol, *Student Member, IEEE*, Brian D. Jeffs, *Senior Member, IEEE*, and
Alle-Jan van der Veen, *Fellow, IEEE*

Abstract—LOFAR is a low-frequency radio astronomical array currently under development in The Netherlands. It is designed to produce synthesis images of the most distant celestial objects yet observed. Due to high redshift levels, observations must be at unusually low frequencies (30–240 MHz), over large apertures (100 km), using thousands of antennas. At these frequencies, Earth’s ionosphere acts as a random refractive sheet which over the large aperture induces source direction dependent gain and phase errors that must be estimated and calibrated out. Current radio astronomy “self-calibration” algorithms do not address direction dependence and will not work in the LOFAR environment. This paper presents a formal study of the parameter estimation problem for LOFAR calibration. A data model is proposed, and a Cramer–Rao lower bound (CRB) analysis is developed with a new general formulation to easily incorporate a variety of constraining signal models. It is shown that although the unconstrained direction dependent calibration problem is ambiguous, physically justifiable constraints can be applied in LOFAR to yield viable solutions. Use of a “compact core” of closely spaced array elements as part of the larger array is shown to significantly improve full array direction dependent calibration performance. Candidate algorithms are proposed and compared to the CRB.

Index Terms—Array calibration, Cramér–Rao bound (CRB), radio astronomy.

NOTATION

k	Subband index, bin centered at f_k Hz, $1 \leq k \leq K$.
m	Short-term integration (STI) time index, bin centered at t_m s. $1 \leq m \leq M$.
$\mathbf{g}_{k,m}^q$	q th column of a matrix $\mathbf{G}_{k,m}$
\mathbf{I}, \mathbf{I}_L	Arbitrary size and $L \times L$ identity matrices, respectively.
$\mathbf{S}_L^{\mathbf{b}}$	$L \times (L - \text{length}\{\mathbf{b}\})$ selection matrix formed by deleting columns specified in \mathbf{b} from \mathbf{I}_L .
$\mathbf{0}, \mathbf{0}_{I,L}$	Arbitrary and $I \times L$ matrix of zeros, respectively.

Manuscript received June 30, 2006; revised December 6, 2006. The associate editor coordinating the review of this manuscript and approving it for publication was Dr. Daniel Fuhrman. This work was supported in part by NWO-STW (The Netherlands) by Grant number DTC.5893, DTC.6478, and by the TU Delft Research Center on ICT. Prior conference publications related to this work are in EUSIPCO, Antalya (T), September 2005, and *Proceedings of the IEEE International Conference on Acoustics, Speech, and Signal Processing (ICASSP)*, May 2006, pp. 1069–1072.

S. van der Tol and A.-J. van der Veen are with the Delft University of Technology (TU), 2628 Delft, The Netherlands (e-mail: S.vanderTol@tudelft.nl; A.J.vanderVeen@tudelft.nl).

B. D. Jeffs is with the Department of Electrical and Computer Engineering, Brigham Young University, Provo, UT 84602 USA (e-mail: bjeffs@ee.byu.edu).

Digital Object Identifier 10.1109/TSP.2007.896243

$\mathbf{1}_L$	$L \times 1$ vector of ones.
$E\{\cdot\}$	Expected value.
$\text{Re}(\cdot), \text{Im}(\cdot)$	Real and imaginary parts, respectively.
$(\cdot)[i, j]$	(i, j) th element of a matrix.
$(\hat{\cdot})$	An estimated quantity.
$(\cdot)^T, (\cdot)^H$	Transpose and Hermitian transpose, respectively.
$\overline{(\cdot)}$	Complex conjugate.
\otimes, \circ	Kronecker matrix product, Khatri–Rao (column-wise Kronecker) product.
$\text{diag}(\cdot)$	Extract diagonal, or build diagonal matrix.
$\text{vec}(\cdot)$	Column scan a matrix to form a vector.
$ \cdot , \angle$	Element-wise absolute value and phase angle.
$\ \cdot\ _F$	Frobenius matrix norm.

I. INTRODUCTION

IN this paper, we study the calibration of a large distributed sensor array. The problem can be phrased as direction-dependent calibration with fewer reference sources than array elements combined with hierarchical beamforming such that not all antenna cross correlations are available at a central location. The reference sources are signals of opportunity that are all simultaneously present. Without further assumptions, the array is not calibratable. As an introduction, we first discuss the instrument and the calibration problem, and then relate this to the existing literature.

A. The LOFAR Radio Telescope

LOFAR is a low frequency radio astronomical array currently under development in The Netherlands by a consortium led by ASTRON. It is designed to produce synthesis images of the most distant (and thus oldest) celestial objects yet observed. Due to high redshift levels, observations must be at unusually low frequencies (30–240 MHz). The current LOFAR design calls for an instrument consisting of nearly 13 000 relatively wide field of view small antennas mounted at ground level. These are grouped into about 72 stations spread in spirals over an area with a diameter of between 100–360 km (depending on funding), as well as in a more densely populated central core. A possible geometry is illustrated in Fig. 1. Each station will have 96 lowband antennas (30–90 MHz, dual-polarized dipoles) and 96 highband “antennas” (110–240 MHz), each consisting of a 16-element dual-polarized beamformed array. Our analysis will concentrate on the lowband system.

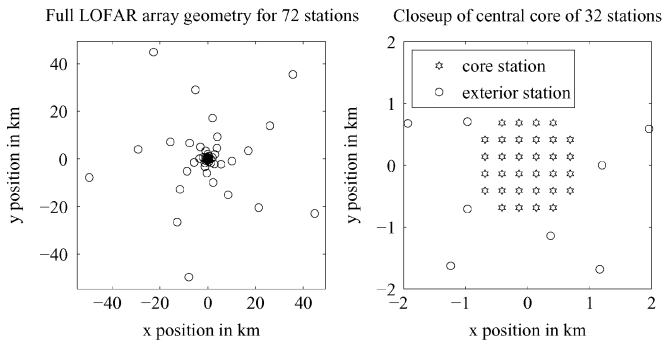


Fig. 1. Possible geometry for the full LOFAR array (left) and the compact central core (right). Each circle or star represents a LOFAR station which acts as a single beamformed directional sensor element in the full array. Initial plans are for five exponentially spaced spiral arms of eight exterior stations each and a compact core of 32 stations.

The 96 antennas in each remote station are used as a phased array and are combined in such a way that a beam is formed into a desired look direction. The resulting output of each beamformer is similar to the output of a telescope dish pointing into the same direction, but is obtained without the use of any moving parts. The beamformer outputs of each station are transported over optical fibers to a central location, where (similar to existing synthesis telescopes [3]–[6]) they are correlated to the outputs of the other stations, and processed into an image.

The design of LOFAR has several challenges, e.g., the sheer computational complexity, and the requirement to achieve a dynamic range of over 70 dB between the strongest and the weakest sources in the final images. The problem which we consider here is the calibration. As a complete problem, it is yet unsolved, and has two levels: a station level and a central (full array) level. This paper focuses primarily on full array calibration, and we study the accuracy of the calibration parameters that can be achieved under various model assumptions.¹

B. LOFAR Calibration

At the station level, each station is expected to form a well-defined beam into a desired direction—this requires accurate estimation of the complex gains of each antenna element in the station array. Available for this is the observed covariance matrix at each station, based on 1-s observations, and a table of the brightest sources in the sky, with known powers and locations. It is further assumed that the antenna elements have known locations and orientations, and “known” antenna patterns (as predicted by EM modeling). We estimate that each complex gain will have an accuracy of only 25 dB (relative to estimation error) [7], and this limits the knowledge and accuracy of the beamshape, in particular at the side lobes.

At the central level, calibration needs to further determine the actual beamshape of each station, and take into account the distortions introduced by the propagation through the ionosphere. The ionosphere is the outer layer of Earth’s atmosphere. Radiation from the sun partly ionizes the atmosphere and the

¹We do not study the accuracy of these models and the resulting estimation bias, nor the effect of the variance of the estimates on the final image. These are open problems.

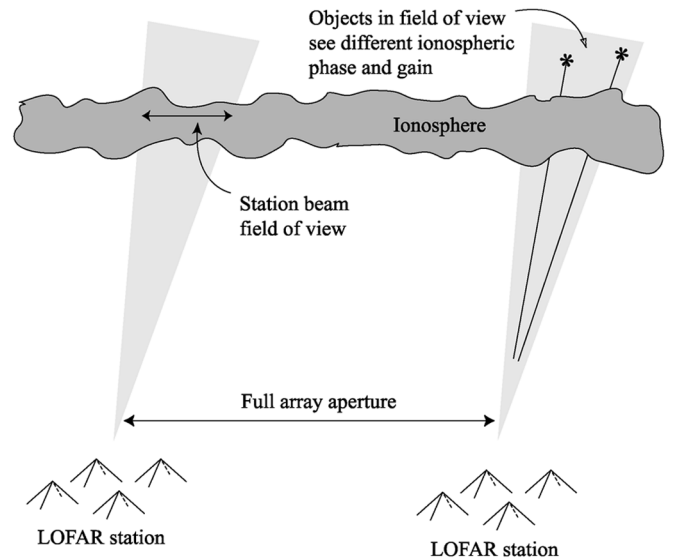


Fig. 2. The problem of LOFAR calibration through ionospheric refraction. Unknown complex gains through the ionosphere are different for each source at each station (after [8]).

resulting free electrons slow down electromagnetic waves propagating through the ionosphere. This additional propagation delay is proportional to the wavelength squared, hence, the corresponding phase shift is proportional to the wavelength. At lower frequencies, the effects of the ionosphere are more severe. Turbulence in the ionosphere causes the electron density to fluctuate both over time (order 10 s) and space (order 10 km).

Fig. 2 illustrates how ionospheric phase and gain perturbations affect LOFAR calibration. The ionospheric irregularity scale is smaller than both the full array aperture and individual station beam field of views, so every station and source direction requires a unique calibration solution. As with station calibration, bright point-like sky sources with known positions are used as “calibrator” references for ionospheric phase and gain estimation.

The initial station calibration should ensure that, within the main lobe, the beamformer response of each station is sufficiently well known. Ionospheric variation across the field of view is gradual enough to permit a low order spatial smoothing model to fit observed perturbations to the known calibrator levels. The known beam response can aid direction dependent calibration and can be factored out so ionospheric gain and phase terms can be isolated.

However, in most observing scenarios there are multiple calibrators outside the mainlobe which are brighter than any source in the beam mainlobe, even after accounting for beamformer attenuation. Furthermore, sidelobe gain and phase responses vary rapidly with arrival angle and depend strongly on electronic instrument calibration variations. Sidelobe response to calibrators must thus be treated as an unknown random quantity which contributes to the direction dependent effect. The array must be accurately calibrated to these bright sources before their corrupting signals can be removed from the imaging array covariance data. This means that a LOFAR calibration algorithm must be capable of joint estimation of independent complex gain terms for every array element (station) and

calibrator source combination. Moreover, at least for the first stages of calibration (used to remove bright sidelobe sources) this must be accomplished without the luxury of a known beam response. The algorithms and analysis presented here address this general case, where known beampatterns are not exploited.

At this stage in the LOFAR development, there is significant uncertainty about how self-calibration algorithms will perform. The radio astronomy community has a wealth of experience in successful synthesis array self-calibration at higher frequencies [3]–[5], [9]. But neither the theoretical or practical bounds on calibration accuracy are well understood for arrays with thousands of antennas spread over a hundred kilometers in the presence of strong ionospheric perturbation. It is not clear whether extensions of existing algorithms will be adequate, and it is likely that new approaches and algorithms will be required [10]. For some observing conditions a sufficiently accurate calibration may be beyond fundamental limits of parameter estimation uncertainty. We propose to answer some of these questions with a thorough Cramér–Rao lower bound (CRB) analysis to determine limiting estimation error variance levels under various model assumptions.

In summary, compared to existing telescopes, LOFAR calibration has the following complications.

- The station beamshapes have significant side lobes; strong sources in the side lobes can dominate weak sources in the main lobe.
- Existing telescopes can calibrate assuming there is one or only a few bright sources in the field of view. For LOFAR, each omnidirectional antenna can see the full sky.
- Each station observes each source through a different patch of the ionosphere. It is easy to see from this that, without further assumptions, the array is not calibratable.

C. Self-Calibration Methods

In the radio astronomy literature, “self-calibration” (or Selfcal) refers to the calibration of a telescope array using existing sky signals as reference sources [3], [5]. It is assumed that these sources have known position and are relatively intense; also the telescope locations/orientations are perfectly known. The parameters to estimate are the direction-independent electronic gains and phases, and the noise powers. Techniques for this have been proposed and are widely used for higher frequency synthesis arrays [11]–[14], and the estimation statistics are well understood [9]. As a refinement, Selfcal is often combined with the well-known CLEAN algorithm for deconvolution [15], [16], i.e., a technique to iteratively estimate the location of the sources and their powers. Generalized Selfcal refers to the poorly studied case where both direction-independent complex gains and direction-dependent propagation effects need to be calibrated [17].

In the array signal processing literature, “self-calibration” (or autocalibration) refers to a much wider class of algorithms, namely calibration using noncooperative sources. Typically, the location of the sources is considered unknown [cf. Direction of Arrival (DOA) estimation]. The additional parameters which need to be estimated can include the direction-independent complex antenna gains or receiver channel mismatch (and more generally the antenna coupling), e.g., [18], [19]. Much less

studied are direction-dependent gains, which may include the individual antenna response, beamshape, and angle-dependent propagation effects [20]. The latter case quickly leads to general models, e.g., to consider the array response matrix to have known gains and unknown phases [21], [22].

A related class of papers (not immediately relevant for LOFAR) also considers estimating or updating the antenna locations along with the other parameters. Many calibration techniques essentially assume the presence of only a single calibration source, or even require a set of calibration sources which can be switched on or separately selected at will. This gives access to the individual uncalibrated array response vectors. Self-calibration as an extension whereby DOA estimation (and, hence, source separation) is alternated with estimating the nuisance parameters. A problem rarely considered in array processing is to assume that many sources are simultaneously present, but that the source covariance matrix is known [23], [7]. This is a relevant assumption in radio astronomy, and LOFAR in particular.

One aspect of LOFAR which is more general than the preceding scenarios is the hierarchical partitioning into stations (or subarrays). In [24] and [25], DOA estimation of partly calibrated arrays with calibrated subarrays are considered. The model in [25] is general and matches the LOFAR context, except that i) the cross correlations between all antenna pairs are observed; ii) the subarrays are perfectly calibrated (for LOFAR this is only approximately the case); and iii) the source locations are unknown.

In summary, the LOFAR calibration problem can be considered as novel in array signal processing.

The paper is organized as follows. Section I-C gives the data model and problem statement. Section II derives the relevant CRBs. Section III proposes calibration algorithms, under various model assumptions and parameter constraints. Section IV shows simulation results. Section V concludes the paper. Prior conference publications providing partial results are in [1] and [2].

D. Signal Model

Each LOFAR station forms steered beams in 1-kHz-wide subbands which track selected deep space objects while their apparent positions shift due to Earth’s rotation. A station beam is treated as a single directional element in the full LOFAR array for processing at the central location; there is no access to the individual elements. Assume all station beams in all subbands for the $J = 72$ stations are steered to the same point in the celestial sphere and that the observed signal is dominated by Q known, bright calibrator point sources. The $J \times 1$ observed array sample vector for the k th subband centered at frequency f_k is

$$\mathbf{x}_k(n) = \sum_{q=1}^Q \mathbf{a}_{k,q}(n) s_{k,q}(n) + \boldsymbol{\eta}_k(n) \quad (1)$$

where $s_{k,q}(n)$ is the signal from the q th calibrator source at time sample n and frequency f_k , $\mathbf{a}_{k,q}(n)$ is the array response vector for this source, and $\boldsymbol{\eta}_k(n)$ is the noise sample vector. $s_{k,q}(n)$ and $\boldsymbol{\eta}_k(n)$ are baseband complex envelope representations of zero mean wide sense stationary white Gaussian random processes

sampled at the Nyquist rate. Elements of $\boldsymbol{\eta}_k(n)$ are statistically independent, as are signals from the Q sources.² For simplicity of presentation all wave propagation is assumed to be nonpolarized. In practice, however, antennas are grouped into orthogonal linear polarization pairs so full Stokes parameter outputs are available to enable observing polarization-specific scientific phenomena. Additionally, calibration parameter estimates must track the effect of ionospheric Faraday rotation. The nonpolarized results presented in this paper are instructive, and extension to a more realistic model is straightforward using Jones matrix notation (cf. [26]), a dual-polarized vector in place of $s_{k,q}(n)$, and extending each array response vector $\mathbf{a}_{k,q}(n)$ to be a two column matrix.

Due to Earth's rotation, the geometrical delay component of $\mathbf{a}_{k,q}(n)$ changes slowly with time, which is a critical feature exploited in synthesis imaging. Calibrator locations and intensities are known accurately from catalogues compiled in previous sky surveys. During calibration all other space signals are neglected due to their relative weakness, but of course their presence can bias the calibration solution.

Let N be the number of time samples in a short-term integration (STI) interval. We assume that $\mathbf{a}_{k,q}(n)$ is (relatively) constant over such an interval, so that, for the m th interval, $\mathbf{x}_k(n)$ is wide sense stationary over $(m-1)N \leq n \leq mN-1$. A single STI autocovariance is defined as

$$\mathbf{R}_{k,m} = E \{ \mathbf{x}_k(n) \mathbf{x}_k^H(n) \} = \mathbf{A}_{k,m} \boldsymbol{\Sigma}_k \mathbf{A}_{k,m}^H + \boldsymbol{\Lambda}_k \quad (2)$$

where $\mathbf{R}_{k,m}$ has size $J \times J$,

$$\begin{aligned} \mathbf{A}_{k,m} &= [\mathbf{a}_{k,1}((m-1)N), \dots, \mathbf{a}_{k,Q}((m-1)N)] \\ \boldsymbol{\Sigma}_k &= \text{diag} \{ [\sigma_{k,1}^2, \dots, \sigma_{k,Q}^2] \} \\ \boldsymbol{\Lambda}_k &= E \{ \boldsymbol{\eta}_k(n) \boldsymbol{\eta}_k^H(n) \} = \text{diag} \{ [\lambda_{k,1}^2, \dots, \lambda_{k,J}^2] \}. \end{aligned}$$

Here, $\sigma_{k,q}^2$ is the variance of the q th calibrator source. Noise is assumed to be independent but not identically distributed across the array, and the noise variances $\lambda_{k,j}^2$ are unknown. In the radio astronomy literature, elements of $\mathbf{R}_{k,m}$ are called "visibilities" [3]. Each visibility represents the interferometric correlation along the baseline vector between the two corresponding array elements. The corresponding short term integration sample covariance estimate is

$$\hat{\mathbf{R}}_{k,m} = \frac{1}{N} \sum_{n=(m-1)N}^{mN-1} \mathbf{x}_k(n) \mathbf{x}_k^H(n).$$

The array response matrix $\mathbf{A}_{k,m}$ can be factored into the product of a phase matrix $\mathbf{K}_{k,m}$ due entirely to the propagation delays associated with the array and source geometry, and a complex calibration gain matrix $\mathbf{G}_{k,m}$ which includes both

²The subband processing in the actual instrument is slightly more subtle than presented here. The stations use 200-kHz subbands. At the central location these signals are time-shifted to compensate for the geometric delays in the look direction, and subsequently split into 1 kHz bins. As a result the narrowband model (1) holds for sources in the look direction, but may not quite hold for sources far outside the field of view. These sources will experience some phase smearing. This effect is not considered in the data model.

source direction dependent ionospheric perturbations and electronic instrumentation gain errors

$$\mathbf{A}_{k,m} = \mathbf{G}_{k,m} \odot \mathbf{K}_{k,m}. \quad (3)$$

In the astronomical literature, the columns of $\mathbf{K}_{k,m}$, denoted by $\mathbf{k}_{k,m}^q$ ($q = 1, \dots, Q$), are often called the "Fourier kernel" and are given by

$$\begin{aligned} \mathbf{k}_{k,m}^q &= \exp \left\{ j \frac{2\pi f_k}{c} \mathbf{Z}^T \mathbf{p}_{m,q} \right\} \\ \mathbf{Z} &= [[x_1, y_1, z_1]^T, \dots, [x_J, y_J, z_J]^T] \end{aligned}$$

where c is the speed of light, $[x_j, y_j, z_j]$ is the position vector for the j th array element (station beam) and $\mathbf{p}_{m,q}$ is a unit length vector pointing in the direction of source q during STI snapshot m . Since \mathbf{Z} , $\mathbf{p}_{m,q}$, and the source power levels are all known to high accuracy for tabulated calibration sources, $\mathbf{K}_{k,m}$ and $\boldsymbol{\Sigma}_k$ are treated as known quantities.

E. Direction Dependent Calibration Formulation

The problem at hand is to estimate $\mathbf{G}_{k,m}$ given $\hat{\mathbf{R}}_{k,m}$ over a range of k and m . $\mathbf{G}_{k,m}$ is in general a $J \times Q$ full matrix of independent unknown complex gain parameters whose elements must be estimated to calibrate the array for imaging. A $(2JQ + J) \times 1$ real parameter vector containing all unknown terms is defined as

$$\begin{aligned} \boldsymbol{\theta}_{k,m} &= [\text{vec}\{|\mathbf{G}_{k,m}|\}^T, \\ &\quad \text{vec}\{\angle \mathbf{G}_{k,m}\}^T, \text{diag}\{\boldsymbol{\Lambda}_k\}^T] \\ &= \left[(\boldsymbol{\gamma}_{k,m}^1)^T, \dots, (\boldsymbol{\gamma}_{k,m}^Q)^T, \right. \\ &\quad \left. (\boldsymbol{\psi}_{k,m}^1)^T, \dots, (\boldsymbol{\psi}_{k,m}^Q)^T, \boldsymbol{\lambda}_k^T \right]^T \end{aligned} \quad (4)$$

where $\boldsymbol{\gamma}_{k,m}^q$ is the q th column of gain matrix $\boldsymbol{\Gamma} = |\mathbf{G}_{k,m}|$, $\boldsymbol{\psi}_{k,m}^q$ is the q th column of phase matrix $\boldsymbol{\Psi} = \angle \mathbf{G}_{k,m}$, and $\boldsymbol{\lambda}_k = \text{diag}\{\boldsymbol{\Lambda}_k\}$. In contrast to LOFAR, the conventional synthesis imaging calibration problem at higher frequencies does not suffer from direction dependent ionospheric perturbations so in this case $\mathbf{G} = \mathbf{g}\mathbf{1}^T$ has the same gain vector \mathbf{g} for each source, and (3) becomes $\mathbf{A} = \text{diag}\{\mathbf{g}\}\mathbf{K}$ [9]. In either case $\boldsymbol{\lambda}$ is a nuisance parameter which must be jointly estimated with \mathbf{G} .

Self-calibration can be viewed as a covariance fitting problem. Substituting (3) into (2) and explicitly showing dependence on $\boldsymbol{\theta}$ yields the visibility measurement equation (ME) [27]

$$\begin{aligned} \text{ME}(\boldsymbol{\theta}_{k,m}) &= (\mathbf{G}(\boldsymbol{\theta}_{k,m}) \odot \mathbf{K}_{k,m}) \\ &\quad \times \boldsymbol{\Sigma}_k (\mathbf{K}_{k,m}^H \odot \mathbf{G}^H(\boldsymbol{\theta}_{k,m})) + \boldsymbol{\Lambda}(\boldsymbol{\theta}_{k,m}). \end{aligned}$$

For a single STI and subband [one (k, m)] the least squares calibration solution follows immediately as

$$\hat{\boldsymbol{\theta}}_{k,m} = \arg \min_{\boldsymbol{\theta}} \|\hat{\mathbf{R}}_{k,m} - \text{ME}(\boldsymbol{\theta})\|_F^2. \quad (5)$$

Direct solution of (5) is not computationally practical. Furthermore it will be shown that without further constraints $\boldsymbol{\theta}_{k,m}$ is not identifiable through a single $\hat{\mathbf{R}}_{k,m}$. The estimation problem

is ill posed and (5) yields ambiguous solutions due to source direction dependence. Fortunately the physics of LOFAR permit imposing structural constraints on individual $\mathbf{G}_{k,m}$ snapshots and/or across a range of time-frequency bins to regularize the problem, as will be shown in sections to follow.

It should also be mentioned that a maximum likelihood (ML) formulation of the LOFAR calibration problem is also easily expressed along the lines of the result in [9]. But, as is often the case, the ML approach does not yield a computationally tractable algorithm for this problem.

II. A FRAMEWORK FOR CRB ANALYSIS

This section presents a general framework for CRB analysis of the source direction dependent calibration gain estimation problem. The approach allows for simple adaptation to a wide range of physically justifiable model assumptions, parameterizations, and signal constraints.

A. CRB for Unconstrained Calibration Parameters

Consider a set of array samples (J stations) observed over a time-frequency domain spanning $1 \leq k \leq K$ frequency bins and $1 \leq m \leq M$ nonoverlapping N sample STI time windows. Stack these samples into an $\text{KMJ} \times N$ data matrix

$$\mathbf{X} = \begin{bmatrix} \mathbf{x}_1(0) & \cdots & \mathbf{x}_1(N-1) \\ \vdots & & \vdots \\ \mathbf{x}_1((M-1)N) & \cdots & \mathbf{x}_1(MN-1) \\ \vdots & & \vdots \\ \mathbf{x}_k((m-1)N) & \cdots & \mathbf{x}_k(mN-1) \\ \vdots & & \vdots \\ \mathbf{x}_K((M-1)N) & \cdots & \mathbf{x}_K(MN-1) \end{bmatrix}.$$

Initially we consider the unstructured case where parameter vectors $\boldsymbol{\theta}_{k,m}$ from each time-frequency bin are distinct with no functional relationship and must all be estimated. These are stacked into a large parameter vector

$$\boldsymbol{\vartheta} = \left[\boldsymbol{\theta}_{1,1}^T, \dots, \boldsymbol{\theta}_{K,1}^T, \dots, \boldsymbol{\theta}_{1,M}^T, \dots, \boldsymbol{\theta}_{K,M}^T \right]^T. \quad (6)$$

The corresponding stacked sample covariance is $\hat{\mathcal{R}} = (1/N)\mathbf{X}\mathbf{X}^H$. The underlying data model is given in (1). Due to Nyquist sampling of narrow passbands selected from the underlying continuous time broadband random signals, both $s_{k,q}(n)$ and $\boldsymbol{\eta}_k(n)$ are statistically independent with respect

to bin indices k and m . All nonzero correlations are spatial (i.e., with respect to station index j) and are due to phase delay across the narrowband array. Thus, the true covariance $\mathcal{R} = E\{\hat{\mathcal{R}}\}$ has block diagonal form

$$\mathcal{R} = \begin{bmatrix} \mathbf{R}_{1,1} & & & & \\ & \ddots & & & \\ & & \mathbf{R}_{K,1} & & \\ & & & \ddots & \\ & & & & \mathbf{R}_{K,M} \end{bmatrix}$$

and \mathcal{R} depends on $\boldsymbol{\vartheta}$ through (2), (3), and (4).

Consider an estimate of $\boldsymbol{\vartheta}$ based on an observation \mathbf{X} . The CRB on the error variance for any unbiased estimator is given by the diagonal elements of

$$\mathcal{C} = \frac{1}{N} \mathcal{M}^{-1}$$

evaluated at the true value of $\boldsymbol{\vartheta}$. Here, \mathcal{M} is the Fisher information matrix, which for Gaussian data can be expressed as [28]

$$\mathcal{M} = \mathcal{J}^H (\overline{\mathcal{R}}^{-1} \otimes \mathcal{R}^{-1}) \mathcal{J} \quad (7)$$

where the Jacobian \mathcal{J} is defined as

$$\mathcal{J} = \frac{\partial \text{vec}(\mathcal{R})}{\partial \boldsymbol{\vartheta}^T}.$$

The matrix $(\overline{\mathcal{R}}^{-1} \otimes \mathcal{R}^{-1})$ is usually very large. However the sparse block diagonal structure for \mathcal{R} in turn makes \mathcal{J} sparse and simplifies evaluation of (7). Thus, \mathcal{M} has the same block diagonal structure as \mathcal{R} , with diagonal blocks given by

$$\mathbf{M}_{k,m} = \mathbf{J}_{k,m}^H \left(\overline{\mathbf{R}}_{k,m}^{-1} \otimes \mathbf{R}_{k,m}^{-1} \right) \mathbf{J}_{k,m}$$

and

$$\mathbf{J}_{k,m} = \left. \frac{\partial \text{vec}(\mathbf{R}_{k,m})}{\partial \boldsymbol{\theta}_{k,m}^T} \right|_{\boldsymbol{\theta} = \boldsymbol{\theta}_{k,m}^{\text{true}}}.$$

With no assumed structure relating parameters across time or frequency, the subblocks of \mathcal{M} are uncoupled and the CRB for some $\hat{\boldsymbol{\theta}}_{k,m}$ can be computed from $\mathbf{M}_{k,m}$ independently from the other parameters. The entries $\mathbf{M}_{k,m}$ are evaluated as follows.

B. Closed Form for General Fisher Information

Using the parameter ordering from (4) each $\mathbf{M}_{k,m}$ can be partitioned into block form as shown in (8) at the bottom of the page.

$$\mathbf{M}_{k,m} = \begin{bmatrix} \mathbf{M}_{\gamma_1 \gamma_1} \cdots \mathbf{M}_{\gamma_1 \gamma_Q} & \mathbf{M}_{\gamma_1 \psi_1} \cdots \mathbf{M}_{\gamma_1 \psi_Q} & \mathbf{M}_{\gamma_1 \lambda} \\ \vdots & \vdots & \vdots \\ \mathbf{M}_{\gamma_Q \gamma_1} \cdots \mathbf{M}_{\gamma_Q \gamma_Q} & \mathbf{M}_{\gamma_Q \psi_1} \cdots \mathbf{M}_{\gamma_Q \psi_Q} & \mathbf{M}_{\gamma_Q \lambda} \\ \mathbf{M}_{\psi_1 \gamma_1} \cdots \mathbf{M}_{\psi_1 \gamma_Q} & \mathbf{M}_{\psi_1 \psi_1} \cdots \mathbf{M}_{\psi_1 \psi_Q} & \mathbf{M}_{\psi_1 \lambda} \\ \vdots & \vdots & \vdots \\ \mathbf{M}_{\psi_Q \gamma_1} \cdots \mathbf{M}_{\psi_Q \gamma_Q} & \mathbf{M}_{\psi_Q \psi_1} \cdots \mathbf{M}_{\psi_Q \psi_Q} & \mathbf{M}_{\psi_Q \lambda} \\ \mathbf{M}_{\lambda \gamma_1} \cdots \mathbf{M}_{\lambda \gamma_Q} & \mathbf{M}_{\lambda \psi_1} \cdots \mathbf{M}_{\lambda \psi_Q} & \mathbf{M}_{\lambda \lambda} \end{bmatrix}. \quad (8)$$

The closed form representation for these submatrices is shown in the Appendix to be

$$\mathbf{M}_{\gamma_p \gamma_q} = 2\sigma_p^2 \sigma_q^2 \text{Re} \left\{ \left(\Phi_p^T \bar{\mathbf{R}}^{-1} \bar{\Phi}_q \right) \left(\mathbf{a}_p^H \mathbf{R}^{-1} \mathbf{a}_q \right) + \left(\Phi_p^T \bar{\mathbf{R}}^{-1} \bar{\mathbf{a}}_q \right) \left(\mathbf{a}_p^H \mathbf{R}^{-1} \Phi_q \right) \right\} \quad (9)$$

$$\mathbf{M}_{\psi_p \psi_q} = 2\sigma_p^2 \sigma_q^2 \text{Re} \left\{ \left(\mathbf{E}_p \bar{\mathbf{R}}^{-1} \bar{\mathbf{E}}_q \right) \left(\mathbf{a}_p^H \mathbf{R}^{-1} \mathbf{a}_q \right) - \left(\mathbf{E}_p \bar{\mathbf{R}}^{-1} \bar{\mathbf{a}}_q \right) \left(\mathbf{a}_p^H \bar{\mathbf{R}}^{-1} \mathbf{E}_q \right) \right\} \quad (10)$$

$$\mathbf{M}_{\lambda \lambda} = \bar{\mathbf{R}}^{-1} \odot \mathbf{R}^{-1} \quad (11)$$

$$\mathbf{M}_{\gamma_p \psi_q} = 2\sigma_p^2 \sigma_q^2 \text{Im} \left\{ \left(\Phi_p^T \bar{\mathbf{R}}^{-1} \bar{\mathbf{E}}_q \right) \left(\mathbf{a}_p^H \mathbf{R}^{-1} \mathbf{a}_q \right) + \left(\Phi_p^T \bar{\mathbf{R}}^{-1} \bar{\mathbf{a}}_q \right) \left(\mathbf{a}_p^H \mathbf{R}^{-1} \mathbf{E}_q \right) \right\} \quad (12)$$

$$\mathbf{M}_{\gamma_q \lambda} = 2\sigma_q^2 \text{Re} \left\{ \Phi_q \bar{\mathbf{R}}^{-1} \circ \mathbf{a}_q^H \mathbf{R}^{-1} \right\} \quad (13)$$

$$\mathbf{M}_{\psi_q \lambda} = -2\sigma_q^2 \text{Im} \left\{ \mathbf{E}_q \bar{\mathbf{R}}^{-1} \circ \mathbf{a}_q^H \mathbf{R}^{-1} \right\} \quad (14)$$

where all terms have implied k, m subscripts and

$$\begin{aligned} \mathbf{E}_q &= \text{diag}(\gamma_q \odot \mathbf{k}_q) \\ \Phi_q &= \text{diag}(\phi_q \odot \mathbf{k}_q) \\ \phi_q &= \exp(j\psi_q). \end{aligned}$$

Since $\mathbf{M}_{\gamma_p \lambda}$ and $\mathbf{M}_{\psi_p \lambda}$ are nonzero, λ is coupled with the parameters of interest and should be jointly estimated.

As will be shown later, in the general case considered here $\mathbf{M}_{k,m}$ is singular. Without introducing constraints on the parameters, the array is not calibratable.

C. CRB for Constrained Parameters

The following sections discuss some scenarios where the degrees of freedom in $\boldsymbol{\vartheta}$ can be reduced by physically justifiable constraining models. These impose structure in \mathcal{R} which is key to solving the calibration problem. At this stage in LOFAR development, there is much activity in identifying appropriate models of ionospheric perturbation effects which can be incorporated into self-calibration algorithms. For example, when the ionosphere is relatively time stable, $\boldsymbol{\theta}_{k,m}$ may vary smoothly over k and m according to some low order interpolation function. In such cases, a lower dimensional parameter vector $\boldsymbol{\rho}$ can represent all the required degrees of freedom over the entire domain of k and m .

Let $\boldsymbol{\vartheta} = f(\boldsymbol{\rho})$ where $f(\cdot)$ is some functional relationship describing a constraint on $\boldsymbol{\vartheta}$ corresponding to an appropriate physical model. It is assumed that $\boldsymbol{\vartheta}$ is an overdetermined parameterization and that the underlying distribution for $\mathbf{x}_k(n)$ is fully determined by $\boldsymbol{\rho}$. Under these conditions, the Fisher information computed for $\boldsymbol{\rho}$ yields the CRB.

Define the constrained Fisher information matrix as

$$\mathcal{M}_{\boldsymbol{\rho}} = \mathcal{J}_{\boldsymbol{\rho}}^H (\bar{\mathbf{R}}^{-1} \otimes \mathbf{R}^{-1}) \mathcal{J}_{\boldsymbol{\rho}} \quad (15)$$

where

$$\mathcal{J}_{\boldsymbol{\rho}} = \frac{\partial \text{vec}(\mathcal{R})}{\partial \boldsymbol{\rho}^T} = \frac{\partial \text{vec}(\mathcal{R})}{\partial \boldsymbol{\vartheta}^T} \frac{\partial f(\boldsymbol{\rho})}{\partial \boldsymbol{\rho}^T} =: \mathcal{J} \mathcal{F} \quad (16)$$

which follows by the chain rule since $\boldsymbol{\vartheta} = f(\boldsymbol{\rho})$. \mathcal{F} can be partitioned as

$$\mathcal{F} = [\mathbf{F}_{1,1}^T, \dots, \mathbf{F}_{K,1}^T, \dots, \mathbf{F}_{1,M}^T, \dots, \mathbf{F}_{K,M}^T]^T$$

where

$$\mathbf{F}_{k,m} = \frac{\partial \boldsymbol{\theta}_{k,m}}{\partial \boldsymbol{\rho}^T}. \quad (17)$$

$\boldsymbol{\rho}$ is common to all time-frequency bins and is not indexed by k or m . Specifying the $\mathbf{F}_{k,m}$ establishes the required structural constraints. Equation (15) can now be written as

$$\mathcal{M}_{\boldsymbol{\rho}} = \mathcal{F}^H [\mathcal{J}^H (\bar{\mathbf{R}}^{-1} \otimes \mathbf{R}^{-1}) \mathcal{J}] \mathcal{F} = \mathcal{F}^H \mathcal{M} \mathcal{F},$$

and since \mathcal{M} is block diagonal

$$\mathcal{M}_{\boldsymbol{\rho}} = \sum_{k=1}^K \sum_{m=1}^M \mathbf{F}_{k,m}^H \mathbf{M}_{k,m} \mathbf{F}_{k,m}. \quad (18)$$

With (18), one may compute a CRB for the constrained parameter vector $\boldsymbol{\rho}$ using the unconstrained general form Fisher matrices given by (8) and constraint Jacobians from (17).

As an illustrative example, consider the simplest time-frequency smoothing function where calibration parameters are constant over k, m . In this case, we can choose $\boldsymbol{\rho} = \boldsymbol{\theta}_{1,1} = \boldsymbol{\theta}_{k,m} \forall (k, m)$, and $\mathbf{F}_{k,m} = \mathbf{I}$. To avoid a singular $\mathcal{M}_{\boldsymbol{\rho}}$ an intrinsic bulk phase ambiguity must be resolved with an additional constraint. Since due to its Hermitian product form $\mathbf{R}_{k,m}$ is unaffected by multiplying any column of $\mathbf{G}_{k,m}$ by a unit modulus scalar, $\angle \mathbf{G}_{k,m}$ can only be known to within one arbitrary phase factor per column. The excess degrees of freedom in $\boldsymbol{\theta}_{k,m}$ can be removed by eliminating the first element of each phase vector $\psi_{k,m}^q$ in $\boldsymbol{\theta}_{k,m}$. This constraint is imposed by setting

$$\boldsymbol{\rho} = \mathbf{S}_L^b \boldsymbol{\theta}_{1,1} = \mathbf{S}_L^b \boldsymbol{\theta}_{k,m}, \quad \forall k, m$$

where $L = (2Q+1)J$ is the number of coefficients in $\boldsymbol{\theta}_{k,m}$, and the selection matrix \mathbf{S}_L^b is formed by deleting the columns from \mathbf{I}_L with indices $\mathbf{b} = [b_1, \dots, b_Q]^T$, $b_q = (q-1+Q)J+1$. This eliminates from $\boldsymbol{\rho}$ the station $j=1$ phase parameter for each of the Q calibrator sources, forcing the first row of \mathbf{G} to be real. It follows that:

$$\mathbf{F}_{k,m} = \mathbf{S}_L^b. \quad (19)$$

The resulting bounds are evaluated in Section IV, along with the performance of the estimation algorithms presented next.

III. CALIBRATION METHODS

A. Single Snapshot Calibration

Above approximately 400 MHz, it is possible for conventional astronomical synthesis imaging arrays to estimate calibration gains from a single ‘‘snapshot’’ STI sample covariance realization $\hat{\mathbf{R}}_{k,m}$ [9], [3]. This is useful for startup of a tracking calibration algorithm or to make quick look snapshot images. In general this is not possible for LOFAR due to directionally dependent ionospheric perturbations.

To illustrate this fact note that for any $Q \times Q$ unitary matrix \mathbf{U} , (2) can be rewritten as

$$\begin{aligned} \mathbf{R} &= \mathbf{A}\boldsymbol{\Sigma}^{\frac{1}{2}}\mathbf{U}\mathbf{U}^H\boldsymbol{\Sigma}^{\frac{1}{2}}\mathbf{A}^H + \boldsymbol{\Lambda} \\ &= \mathbf{A}\boldsymbol{\Sigma}^{\frac{1}{2}}\mathbf{U}\boldsymbol{\Sigma}^{-\frac{1}{2}}(\boldsymbol{\Sigma}^{-\frac{1}{2}})^H\mathbf{U}^H\boldsymbol{\Sigma}^{\frac{1}{2}}\mathbf{A}^H + \boldsymbol{\Lambda} \\ &= \tilde{\mathbf{A}}\tilde{\mathbf{A}}^H + \boldsymbol{\Lambda} \end{aligned} \quad (20)$$

where $\tilde{\mathbf{A}} = \mathbf{A}\boldsymbol{\Sigma}^{(1)/(2)}\mathbf{U}\boldsymbol{\Sigma}^{-(1)/(2)}$. Since $\mathbf{U}\mathbf{U}^H = \mathbf{I}$, it is not visible in \mathbf{R} . However, (20) has the same structure as (2) but with a different effective array response, $\tilde{\mathbf{A}}$. Thus, each choice of \mathbf{U} leads to a different calibration solution $\tilde{\mathbf{G}}$, namely (using $\tilde{\mathbf{A}} = \tilde{\mathbf{G}} \odot \mathbf{K}$),

$$\tilde{\mathbf{G}} = (\mathbf{A}\boldsymbol{\Sigma}^{\frac{1}{2}}\mathbf{U}\boldsymbol{\Sigma}^{-\frac{1}{2}}) \odot \mathbf{K}^{\odot -1} \quad (21)$$

where $(\cdot)^{\odot -1}$ denotes element-wise inverse. This shows that, without adding constraints, \mathbf{A} is not identifiable from a single $\hat{\mathbf{R}}_{k,m}$. (This problem is not present in the classical direction-independent calibration problem, where $\mathbf{G} = \mathbf{g}\mathbf{1}^T$, or $\mathbf{A} = \text{diag}\{\mathbf{g}\}\mathbf{K}$ [9].)

Next, we introduce a physically justifiable constraint based on the unique LOFAR array geometry which resolves this ambiguity so that with sufficient signal-to-noise ratio (SNR) a calibration can be computed already from a single snapshot $\hat{\mathbf{R}}_{k,m}$. Subsequently, in Section III-C, we consider multiple snapshots and make assumptions on the time evolution of the ionosphere.

B. Exploiting the Compact Core LOFAR Geometry

The unknown calibration gains/phases can be attributed to perturbations due to (a) the propagation through the ionosphere, and (b) the receiver electronics. The ionosphere mostly introduces propagation delays, i.e., it can be modeled as a random phase sheet, with gains that are approximately direction independent over a station main beam. Similarly, the electronic gains and phases are independent of the directions to the calibration sources, but do differ from station to station.

The planned geometry for LOFAR as shown in Fig. 1 includes a central core of J_c closely packed stations. As shown in Fig. 3, the core subarray is operating in a regime where the station beam fields of view overlap on the ionosphere (approximately 300 km above the array). These beam mainlobe ‘‘footprints’’ are much larger than, and the total subarray aperture is much smaller than the ionospheric irregularity scale [8]. Thus each core station observes a given celestial source through the same patch of ionosphere and sees a common gain-phase perturbation, i.e., the core subarray sees a coherent scene without direction dependence.

Because they are common, the ionospheric phases cancel out when computing the correlations $\mathbf{R}_{k,m}$ for the core subarray. What remains is the direction-independent ionospheric gains, and the gains/phases of the receiver electronics. The corresponding core gain matrix \mathbf{G}_c can be modeled as $\mathbf{G}_c = \mathbf{g}_c\mathbf{1}^T$.

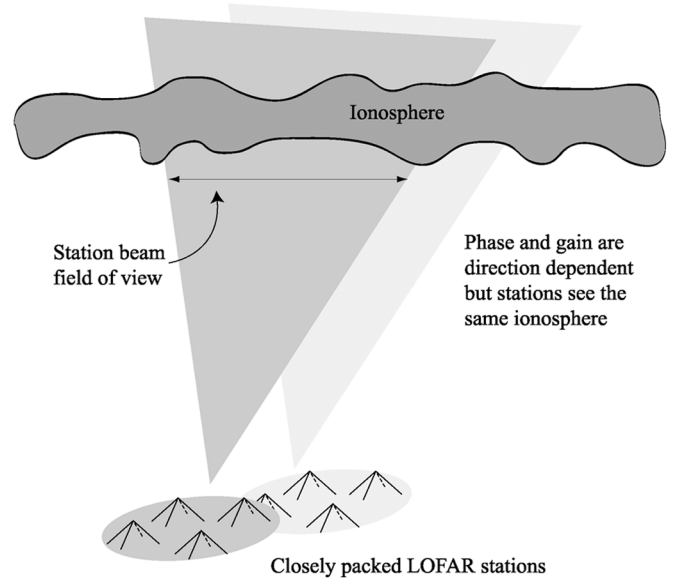


Fig. 3. Calibration scenario for closely spaced LOFAR central core stations. Due to beam overlap at ionospheric altitude, each station sees the same direction dependence. (After C. Lonsdale.)

This leads to a calibration problem comparable to the typical synthesis imaging situation at higher frequencies (or similar to station calibration).

For the rest of the array, i.e., for the $J_e = J - J_c$ stations exterior to the core, both the field of view and all interelement baselines are greater than the ionospheric irregularity scale, as shown in Fig. 2. For these stations the corresponding gain matrix \mathbf{G}_e is best modeled as a full matrix.

Under these assumptions, (3) becomes

$$\begin{aligned} \mathbf{A} &= \mathbf{G} \odot \mathbf{K} = \begin{bmatrix} \mathbf{G}_c \odot \mathbf{K}_c \\ \mathbf{G}_e \odot \mathbf{K}_e \end{bmatrix} \\ &= \begin{bmatrix} \text{diag}\{\mathbf{g}_c\}\mathbf{K}_c \\ [\mathbf{g}_e^1 \odot \mathbf{k}_e^1, \dots, \mathbf{g}_e^Q \odot \mathbf{k}_e^Q] \end{bmatrix} \end{aligned}$$

(the implied (k, m) indices are omitted). To bring all calibration gain vectors to be estimated into a single indexing scheme, let $q = 0$ refer to the central core, and define

$$\begin{aligned} \tilde{\mathbf{g}}_q &= \begin{cases} \mathbf{g}_c, & \text{for } q = 0, \\ \mathbf{g}_e^q, & \text{for } 1 \leq q \leq Q \end{cases} \\ \boldsymbol{\rho} &= [\tilde{\mathbf{g}}_0^T, \dots, \tilde{\mathbf{g}}_Q^T, \angle \tilde{\mathbf{g}}_0^T, \dots, \angle \tilde{\mathbf{g}}_Q^T, \boldsymbol{\lambda}^T]^T. \end{aligned} \quad (22)$$

Here, $\tilde{\mathbf{g}}_0$ corresponding to the single core subarray gain vector is length J_c , while the $\tilde{\mathbf{g}}_q$ are length J_e .

The constraint Jacobian, shown in (23) at the bottom of the page, expresses the relationship between $\boldsymbol{\rho}$ in (22) and $\boldsymbol{\theta}_{k,m}$ in

$$\mathbf{F}_{k,m} = \begin{bmatrix} \mathbf{1}_Q \otimes \begin{bmatrix} \mathbf{I}_{J_c} \\ \mathbf{0}_{J_c, J_c} \end{bmatrix} & \mathbf{I}_Q \otimes \begin{bmatrix} \mathbf{0}_{J_c, J_c} \\ \mathbf{I}_{J_c} \end{bmatrix} & \mathbf{0} & \mathbf{0} & \mathbf{0} \\ \mathbf{0} & \mathbf{0} & \mathbf{1}_Q \otimes \begin{bmatrix} \mathbf{I}_{J_c} \\ \mathbf{0}_{J_c, J_c} \end{bmatrix} & \mathbf{I}_Q \otimes \begin{bmatrix} \mathbf{0}_{J_c, J_c-1} \\ \mathbf{S}^b_{J_c} \end{bmatrix} & \mathbf{0} \\ \mathbf{0} & \mathbf{0} & \mathbf{0} & \mathbf{0} & \mathbf{I}_M \end{bmatrix}. \quad (23)$$

(4). It also constrains the bulk phase ambiguity as does (19), by setting $\mathbf{b} = [1]$ to omit the phase on the first external station. Using (23) in (18) for a single snapshot (k, m) gives $\mathcal{M}_\rho = \mathbf{F}_{k,m}^H \mathbf{M}_{k,m} \mathbf{F}_{k,m}$, and yields a closed form CRB for a LOFAR array with a central core. This has been used to evaluate the CRB for a wide range of scenarios, and leads to the following observations:

- 1) \mathbf{M}_ρ is typically singular when $J_c < Q - 1$.
- 2) When $J_c \geq Q - 1$ the full array, including the fully direction dependent ionospheric gains in the exterior stations can be reliably calibrated with a single snapshot sample covariance.

Currently, the number of central compact core stations is planned as $J_c = 32$. Thus, single snapshot calibration exploiting the core configuration is suitable if Q represents a small number of bright calibrator sources, i.e., for initial coarse calibration.

C. Exploiting Frequency-Time Diversity

We will now consider the use of multiple snapshots. The ionospheric parameters are approximately constant over a block of (k, m) values covering 10 s and 500 kHz. Due to Earth's rotation and frequency dependence, $\mathbf{K}_{k,m}$ varies sufficiently over this block so that, even if the individual $\mathbf{M}_{k,m}$ are singular, the sum in (18) produces a full rank \mathcal{M}_ρ and a relatively low CRB.

For regions larger than a 10 s \times 500 kHz block, $\mathbf{G}_{k,m}$ generally varies smoothly. It is, therefore, unnecessary to compute independent estimates for each $\theta_{k,m}$. A low-order smoothing function can describe the significant variations with fewer parameters and thus lower estimation error variance. For example, we can use separate matrix polynomials in f , t , and coefficient vector ρ for the phase matrix Ψ an gain matrix Γ and evaluate them at STI frequency-time bin (k, m) as follows:

$$\mathbf{G}_{k,m}(\rho) = [\Gamma(\rho, f, t) \odot \exp\{j\Psi(\rho, f, t)\}]|_{f=f_k, t=t_k} \quad (24)$$

$$\begin{aligned} \Gamma(\rho, f, t) &= \sum_{d=1}^D \mathbf{Y}_d f^{\kappa_d} t^{\mu_d}, \quad \Psi(\rho, f, t) = \sum_{d=1}^D \mathbf{T}_d f^{\kappa_d} t^{\mu_d} \\ \rho &= \text{vec}[\mathbf{Y}_1, \dots, \mathbf{Y}_D, \mathbf{T}_1, \dots, \mathbf{T}_D, \boldsymbol{\lambda}]. \end{aligned} \quad (25)$$

\mathbf{Y}_d and \mathbf{T}_d are the $J \times Q$ gain and phase coefficient matrices, to be estimated by calibration. To illustrate the notation, consider a specific example for the phase polynomial

$$\Psi(\rho, f, t) = \mathbf{T}_1 + \mathbf{T}_2 f + \mathbf{T}_3 t + \mathbf{T}_4 f t + \mathbf{T}_5 f^2$$

which consists of $D = 5$ terms, using powers for f as $\{\kappa_1, \dots, \kappa_5\} = \{0, 1, 0, 1, 2\}$ and for t as $\{\mu_1, \dots, \mu_5\} = \{0, 0, 1, 1, 0\}$.

The dual (gain and phase) polynomial model combined with the bulk phase ambiguity resolution used in (19) results in the

following constraint Jacobian: [see (26) at the bottom of the page], where $L = JQ$ and $\mathbf{B} = \mathbf{I}_Q \otimes \mathbf{S}_J^b$, $\mathbf{b} = [1]$. It is straightforward to combine this with the assumption of a central core geometry (Section III-B). In this case, $\mathbf{F}_{k,m}$ is given by the product of (23) and (26), but using $L = QJ_e + J_c$ and $\mathbf{B} = \mathbf{I}_{Q(J_e-1)+J_c}$.

A least squares solution for ρ can be expressed as

$$\hat{\rho} = \arg \min_{\rho} \sum_{k=0}^{K-1} \sum_{m=0}^{M-1} \|\hat{\mathbf{R}}_{k,m} - \text{ME}_{k,m}(\rho)\|_F^2 \quad (27)$$

where

$$\begin{aligned} \text{ME}_{k,m}(\rho) &= (\mathbf{G}_{k,m}(\rho) \odot \mathbf{K}_{k,m}) \\ &\quad \times \Sigma_k(\mathbf{K}_{k,m}^H \odot \mathbf{G}_{k,m}(\rho)^H) + \boldsymbol{\Lambda}_k(\rho). \end{aligned} \quad (28)$$

Although the polynomial model dramatically reduces parameter degrees of freedom and (26) yields a low CRB, a direct implementation of (27) is computationally impractical. An iterative search algorithm is required but its convergence performance is poor. The continuous phase polynomial $\Psi(\rho, f, t)$ is ambiguous to integer multiples of 2π at every evaluation point, i.e., for every combination of station j , source q , f_k , and t_m . This introduces many local minima so that a good initial estimate for ρ is required. The following two sections present algorithms which address these problems.

D. The Peeling Algorithm

The current leading candidate algorithm for LOFAR calibration was introduced in [10] and has been dubbed ‘‘Peeling’’ due its sequential approach of successively calibrating on one bright source at a time followed by removing (peeling) that source's contribution from the observed sample covariances, $\hat{\mathbf{R}}_{k,m}$. Peeling is based on three basic simplifying assumptions as follows.

- Joint estimation for parameters of all Q calibrators sources can be approximated with a series of single source calibration problems, in descending order of source brightness.
- Calibration gains vary slowly and smoothly over time and frequency. Consequently, over some span of K_b frequency bins and M_b time bins called a ‘‘block,’’ $\mathbf{G}_{k,m}$ is approximately constant. This block indexed by (\tilde{k}, \tilde{m}) includes all frequency-time (STI) bins in the set

$$\mathcal{B}_{\tilde{k}, \tilde{m}} = \{(k, m) : \tilde{k}K_b \leq k \leq (\tilde{k} + 1)K_b - 1, \tilde{m}M_b \leq m \leq (\tilde{m} + 1)M_b - 1\}$$

The evolution of the ionospheric gains over several blocks (a ‘‘domain’’) is described by a polynomial model as in (28).

- Within a block, the variations in $\mathbf{K}_{k,m}$ (also known as fringe rotations) due to Earth's rotation and frequency change are large. Source powers $\sigma_{k,q}^2$ are constant over k within a block.

$$\mathbf{F}_{k,m} = \begin{bmatrix} f_k^{\kappa_1} t_m^{\mu_1} \mathbf{I}_L & \dots & f_k^{\kappa_D} t_m^{\mu_D} \mathbf{I}_L & \mathbf{0} & \dots & \mathbf{0} & \mathbf{0} \\ \mathbf{0} & \dots & \mathbf{0} & f_k^{\kappa_1} t_m^{\mu_1} \mathbf{B} & \dots & f_k^{\kappa_D} t_m^{\mu_D} \mathbf{B} & \mathbf{0} \\ \mathbf{0} & \dots & \mathbf{0} & \mathbf{0} & \dots & \mathbf{0} & \mathbf{I}_J \end{bmatrix} \quad (26)$$

Peeling in [10] does not use the central core geometry assumption.

Let $\boldsymbol{\rho}$ be a minimal parameterization for the calibration parameters. Define $\boldsymbol{\rho}_q$ as the subvector of $\boldsymbol{\rho}$ corresponding to the parameters for source q , i.e., corresponding to the q th columns from $\mathbf{Y}_1, \dots, \mathbf{Y}_D$ and $\mathbf{T}_1, \dots, \mathbf{T}_D$ in the polynomial model (25). The corresponding gain vector for STI bin (k, m) is given by the vector polynomial $\mathbf{g}_{k,m}^q = \mathbf{g}_{k,m}(\boldsymbol{\rho}_q)$, which is also obtained by retaining only the q th columns from $\boldsymbol{\Gamma}(\boldsymbol{\rho}, f, t)$ and $\boldsymbol{\Psi}(\boldsymbol{\rho}, f, t)$ in (24). No superscript q is used in $\mathbf{g}_{k,m}(\boldsymbol{\rho}_q)$ since all column-wise polynomials are identical except for the source dependent coefficients in each $\boldsymbol{\rho}_q$. Similarly, $\mathbf{v}_{k,m}^q$ denotes the q th column of $\mathbf{K}_{k,m}$, and contains the geometric phase delays of source q . Finally, $\hat{\boldsymbol{\rho}}_p$ will denote the current parameter vector estimate for a single source p .

Assuming the Q sources are ordered in descending brightness, an I pass peeling algorithm based on [10] is given by

- 1) *Initialize*: source index $q = 1$, pass index $i = 1$, and parameter vector $\hat{\boldsymbol{\rho}}_p = \mathbf{0}$ for $1 \leq p \leq Q$.
- 2) *Update the residuals (peel)*: Over all (k, m) covering all blocks in the domain, subtract from each sample covariance the current best estimates (based on $\hat{\boldsymbol{\rho}}_p, 1 \leq p \leq Q, p \neq q$) of contributions from all except the q th source:

$$\hat{\mathbf{V}}_{k,m,q} = \hat{\mathbf{R}}_{k,m} - \sum_{\substack{p=1 \\ p \neq q}}^Q \left(\mathbf{g}_{k,m}(\hat{\boldsymbol{\rho}}_p) \odot \mathbf{k}_{k,m}^p \right) \sigma_{k,p}^2 \left(\mathbf{g}_{k,m}(\hat{\boldsymbol{\rho}}_p) \odot \mathbf{k}_{k,m}^p \right)^H.$$

$\hat{\mathbf{V}}_{k,m,q}$ is an estimate of the visibility (covariance) matrix contribution to $\hat{\mathbf{R}}_{k,m}$ from source q . The term under the summation is a single source version of (28). The noise covariance $\boldsymbol{\Lambda}$ is neglected.

- 3) *Phase center and average*: For each $\hat{\mathbf{V}}_{k,m,q}$, cancel the phase rotation due to the geometric delay term $\mathbf{k}_{k,m}^q$ in the visibility contribution from source q . Then average over (k, m) inside a block $\mathcal{B}_{\tilde{k}, \tilde{m}}$ to attenuate the other, noncentered, sources,

$$\hat{\mathbf{V}}_{\tilde{k}, \tilde{m}, q} = \frac{1}{K_b M_b} \sum_{(k,m) \in \mathcal{B}_{\tilde{k}, \tilde{m}}} \text{diag} \left\{ \bar{\mathbf{k}}_{k,m}^q \right\} \times \hat{\mathbf{V}}_{k,m,q} \text{diag} \left\{ \mathbf{k}_{k,m}^q \right\}. \quad (29)$$

- 4) *Estimate polynomial coefficients*: With some abuse of notation, let the subscript (\tilde{k}, \tilde{m}) on $\mathbf{g}_{\tilde{k}, \tilde{m}}^q$ denote selecting the (k, m) frequency-time bin in the center of block (\tilde{k}, \tilde{m}) , and likewise for $\sigma_{\tilde{k}, q}^2$. Then assume a single-source model and estimate the polynomial coefficients for source q as

$$\hat{\boldsymbol{\rho}}_q = \arg \min_{\boldsymbol{\rho}_q} \sum_{(\tilde{k}, \tilde{m})} \left\| \mathbf{L} \odot \left(\hat{\mathbf{V}}_{\tilde{k}, \tilde{m}, q} - \sigma_{\tilde{k}, q}^2 \mathbf{g}_{\tilde{k}, \tilde{m}}(\boldsymbol{\rho}_q) \left(\mathbf{g}_{\tilde{k}, \tilde{m}}(\boldsymbol{\rho}_q) \right)^H \right) \right\|_{\mathbf{F}}^2.$$

\mathbf{L} is a masking matrix of ones below the diagonal and zeros elsewhere which is used to avoid fitting to diagonal terms from $\boldsymbol{\Lambda}$. This problem is solved using a general least squares solver.

- 5) *Iterate* for $q = 1, \dots, Q$ and do this for I passes.

We have found that using multiple passes (e.g., $2 \leq I \leq 5$) reduces bias in $\hat{\boldsymbol{\rho}}_q$ which arises when the averaging over a block in step 3 produces insufficient attenuation of the non centered sources. Contamination in the single source fit in step 4 occurs because $\hat{\mathbf{V}}_{\tilde{k}, \tilde{m}, q}$ has contributions from more than the centered source. The next section presents a more direct method of reducing this bias.

E. Demixing Calibrator Cross Contamination

The purpose of steps 2 and 3 is to form a single-source approximation of the problem. Ideally $\hat{\mathbf{V}}_{\tilde{k}, \tilde{m}, q}$ is equal to the true single source phase centered visibility $\mathcal{V}_{k,m,q}$ for sample (k, m) at the center of block (\tilde{k}, \tilde{m}) . Assuming the gains $\mathbf{g}_{k,m}(\boldsymbol{\rho}_q)$ and source powers $\sigma_{k,q}^2$ are constant within the block gives

$$\mathcal{V}_{\tilde{k}, \tilde{m}, q} = \sigma_{k,q}^2 \mathbf{g}_{k,m}^q(\boldsymbol{\rho}_q) \left(\mathbf{g}_{k,m}(\boldsymbol{\rho}_q) \right)^H \quad \forall (k, m) \in \mathcal{B}_{\tilde{k}, \tilde{m}} \quad (30)$$

(the additive noise is ignored). Initially, when estimating the parameters for source q there are no available estimates for sources $q+1$ to Q , so their contribution cannot be subtracted in step 2. Averaging in step 3 is then not sufficient to reduce bias down to the noise level and multiple iterations are necessary.

In this section, we develop an unbiased estimator $\hat{\mathbf{V}}_{\tilde{k}, \tilde{m}, q}$ so that even on the first pass $E\{\hat{\mathbf{V}}_{\tilde{k}, \tilde{m}, q}\} \approx \mathcal{V}_{\tilde{k}, \tilde{m}, q}$. The algorithm works on a per block basis, so for notational simplicity the block indices (\tilde{k}, \tilde{m}) will be dropped, and we take the ranges $k = 1, \dots, K_b, m = 1, \dots, M_b$ (a single block).

Consider estimating $\boldsymbol{\rho}_q$ during the first peeling pass. Estimates $\hat{\boldsymbol{\rho}}_p$ for $1 \leq p < q$ will have been previously computed, and we assume that the corresponding sources are peeled without bias in step 2. We now seek an estimate $\hat{\boldsymbol{\rho}}_q$ which is unbiased by the presence of sources $q+1$ to Q in $\hat{\mathbf{R}}_{k,m}$. These sources have not yet been peeled since at this stage $\hat{\boldsymbol{\rho}}_p = \mathbf{0}$ for $p = q+1, \dots, Q$. The expected value of entry i, j from $\hat{\mathbf{V}}_{k,m,q}$ in step 2 can then be expressed as (for $i, j = 1, \dots, J$)

$$E\{\hat{\mathbf{V}}_{k,m,q}[i, j]\} = \sum_{p=q}^Q \mathbf{k}_{k,m}^p [i] \bar{\mathbf{k}}_{k,m}^p [j] \nu_{p,ij} \quad \nu_{p,ij} = \sigma_p^2 \mathbf{g}_p [i] \bar{\mathbf{g}}_p [j] \quad (31)$$

where $\mathbf{g}_q = \mathbf{g}_{k,m}(\boldsymbol{\rho}_q)$ and $\sigma_q^2 = \sigma_{k,q}^2$ are constant within a block. The summation can be written as

$$E\{\hat{\mathbf{V}}_{k,m,q}[i, j]\} = \left[\mathbf{k}_{k,m}^q [i] \bar{\mathbf{k}}_{k,m}^q [j], \dots, \mathbf{k}_{k,m}^Q [i] \bar{\mathbf{k}}_{k,m}^Q [j] \right] \boldsymbol{\nu}_{ij} \quad \boldsymbol{\nu}_{ij} = [\nu_{q,ij}, \dots, \nu_{Q,ij}]^T. \quad (32)$$

This gives us one equation per (k, m) pair in the block $\mathcal{B}_{\tilde{k}, \tilde{m}}$. To stack these into a matrix, let

$$\mathcal{K}_{ij} = \begin{bmatrix} \mathbf{k}_{1,1}^q [i] \bar{\mathbf{k}}_{1,1}^q [j] & \cdots & \mathbf{k}_{1,1}^Q [i] \bar{\mathbf{k}}_{1,1}^Q [j] \\ \vdots & \ddots & \vdots \\ \mathbf{k}_{K_b, M_b}^q [i] \bar{\mathbf{k}}_{K_b, M_b}^q [j] & \cdots & \mathbf{k}_{K_b, M_b}^Q [i] \bar{\mathbf{k}}_{K_b, M_b}^Q [j] \end{bmatrix}$$

(size $K_b M_b \times Q - q + 1$) and

$$\hat{\boldsymbol{\nu}}_{ij} = [\hat{\mathbf{V}}_{1,1,q}[i, j], \dots, \hat{\mathbf{V}}_{K_b, M_b, q}[i, j]]^T.$$

then (31) becomes $E\{\hat{\mathbf{v}}_{ij}\} = \mathcal{K}_{ij}\mathbf{v}_{ij}$. If \mathcal{K}_{ij} is a “tall” matrix, which requires (for $q = 1$) $K_b M_b \geq Q$, then it will be left-invertible. Applying the left inverse to both sides of the equation, we obtain

$$E\left\{\left(\mathcal{K}_{ij}^H \mathcal{K}_{ij}\right)^{-1} \mathcal{K}_{ij}^H \hat{\mathbf{v}}_{ij}\right\} = \mathbf{v}_{ij}. \quad (33)$$

The least squares estimator for \mathbf{v}_{ij} given $\hat{\mathbf{v}}_{ij}$ is

$$\hat{\mathbf{v}}_{ij} = \left(\mathcal{K}_{ij}^H \mathcal{K}_{ij}\right)^{-1} \mathcal{K}_{ij}^H \hat{\mathbf{v}}_{ij} \quad (34)$$

which is shown by (33) to be unbiased. Comparing (30) with (31)–(32) reveals that the first element of $\hat{\mathbf{v}}_{ij}$ is the estimator we seek for $\hat{V}_{\tilde{k}, \tilde{m}, q}[i, j]$. Equation (34) is separately computed for each (i, j) to yield full matrix $\hat{V}_{\tilde{k}, \tilde{m}, q}$ for use in Peeling step 4.

A closer look at (34) reveals that it is directly related to the original peeling approach of phase centering and averaging. First define

$$\mathbf{C}_{ij} = K_b M_b (\mathcal{K}_{ij}^H \mathcal{K}_{ij})^{-1}.$$

Now we can write

$$\hat{\mathbf{v}}_{ij} = \mathbf{C}_{ij} \left[\frac{1}{K_b M_b} \mathcal{K}_{ij}^H \hat{\mathbf{v}}_{ij} \right].$$

Comparing this matrix equation with the summation of (29) reveals that the first element of the term in brackets is equal to the (i, j) th element of $\hat{V}_{\tilde{k}, \tilde{m}, q}$ from (29). The remaining elements correspond to evaluating (29) for sources $q + 1$ to Q . Thus computing $(1)/(K_b M_b) \mathcal{K}_{ij}^H \hat{\mathbf{v}}_{ij}$ performs an element-wise version of the Peeling phase centering and averaging step on not just q , but for all sources q to Q . The multiplication by inversion matrix \mathbf{C}_{ij} “demixes” the contributions of the sources into separate single source problems.

The estimates $\hat{\rho}_p$ in step 4 are based on all samples in the domain. The demixing algorithm works only on a single block. Therefore demixing is noisier than removing a source by conventional Peeling subtraction. The noise amplification depends on the condition of \mathbf{C}_{ij} . Because of the third assumption of Section III-D (large fringe rotations within a block) \mathbf{C}_{ij} will be well conditioned. For large blocks, \mathbf{C}_{ij} will converge to the identity matrix.

IV. SIMULATION RESULTS

A. CRB for Constant Calibration Gains and Phases

We first consider estimating calibration parameters over a small frequency-time block where they can be assumed constant. Fig. 4 illustrates the CRB for a realistic self-calibration scenario with the full LOFAR geometry of Fig. 1. Station beams are pointed at right ascension (RA) 54.0° and declination (DEC) 55.1° .³ An accurate model based on the existing LOFAR initial test station [29] was used for the station beam directional response, including sidelobe fine structure. For this 40-MHz observation, the -3 dB beamwidth is approximately 5° with sidelobe peak levels typically at -13 dB below the mainlobe.

³RA and DEC are astronomical polar coordinates for fixed locations in the celestial sphere used to locate deep space objects; the celestial equivalent of latitude and longitude. See, e.g., <http://liftoff.msfc.nasa.gov/academy/universe/radec.html>.

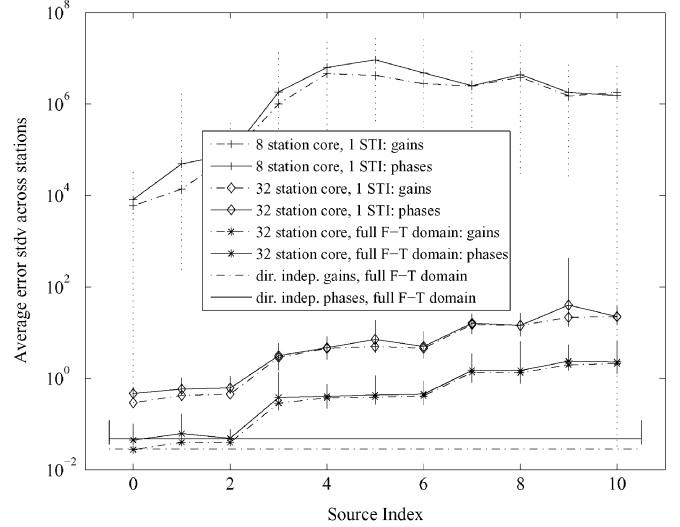


Fig. 4. Calibration CRB levels for constant parameters over small frequency-time span. Curves are CRB values averaged across array elements (stations) to provide a representative error level per source. Vertical bars show the range of phase errors across the 72 stations. Phase error is in radians while gain error is unitless. “Source 0” corresponds to the compact subarray which does not have source dependent calibration. Bottom horizontal curves are given as a reference for the case where calibration parameters are not source direction dependent.

TABLE I
TEN BRIGHTEST CALIBRATOR SOURCES

Source	Catalog Name	RA ^o	DEC ^o	SNR dB
1	3C461	350.8	58.8	-20.7
2	3C405	299.9	40.7	-21.0
3	3C86	51.8	55.3	-30.0
4	3C144	83.6	22.0	-31.6
5	3C274	187.7	12.4	-31.6
6	3C123	69.3	29.7	-31.9
7	4C+53.06	52.5	53.6	-37.2
8	4C+53.07	54.1	53.6	-37.2
9	3C33	17.2	13.3	-38.7
10	4C+55.07	53.1	55.9	-39.1

The $Q = 10$ brightest radio sources after beamforming are included in the simulation. Table I lists their locations, taken from the standard 3C and 4C radio survey catalogues [30], and apparent SNRs computed from tabulated flux values. Sources 3, 7, 8, and 10 are seen within the beam mainlobe. Random “true” calibration parameters were generated using Gaussian gain magnitudes with a mean of 1.0 and standard deviation of 0.3, and phases uniformly distributed in the range $[-\pi, \pi]$.

The curves marked with a diamond in Fig. 4 show the CRB as function of source index for calibration on a single STI snapshot, using the central core configuration ($J_c = 32$ central core stations). The CRB is computed using (18), with constraint Jacobian $\mathbf{F}_{k,m}$ from (23). The “asterisk” curves show the same for $K = 11$ frequency bins and $M = 10$ time snapshots, covering 110 STI snapshots on a sample grid with one second by 50-kHz spacing. (As with all results in Section IV, we assume narrowband array operation with frequency bins sufficiently narrow that no phase smearing occurs in visibility es-

timates. The 50-kHz bin spacing exceeds the narrowband limit, so we assume individual bins are more narrow, but selected at widely separated frequencies to reduce computational burden). The resulting region of 10 s by 500 kHz is considered to be the maximum span that can be assumed to have constant calibration parameters. In both the single snapshot and 10 s \times 500 kHz cases, the use of the direction independent calibration model for the central core leads to low calibration error bounds for the first few sources. The error increases with the source index, as the source SNR decreases, and after the sixth source (third for middle single STI curves) unacceptable phase errors of more than one radian are encountered. Useful calibration for the remaining sources requires a region larger than 10 s by 500 kHz.

The top curves show the bounds for $J_c = 8$ central core stations, modeling the other 24 core stations as external stations. Since this is smaller than $Q - 1$, the calibration error becomes extremely large. The horizontal curves at the bottom are provided as a reference, and represent CRB values for the same 10 source case but where calibration parameters do *not* depend on source direction, i.e., only one complex parameter must be estimated for each station. This represents the conventional synthesis imaging problem at higher frequencies where ionospheric interaction is not strong or the aperture is smaller. The comparison illustrates the relative difficulty of direction dependent calibration, particularly for weaker sources.

B. CRB for Polynomial Calibration Variation

Large STI regions are needed to improve the CRB performance with direction dependent calibration. The parameters are not constant over such regions but vary smoothly, and the polynomial calibration models discussed in Section III-C will be used. To reduce the sizable computational and memory requirements, a “thinned” LOFAR array is used in all simulations to follow. Every second element from Fig. 1 was included, with $J = 36$ stations covering the 100-km aperture and with a central core of $J_c = 16$ stations.

In the first experiment, shown in Fig. 5, a basic setup without central core assumption is used, so an independent frequency-time polynomial is applied for each source-station combination. A first order in both time and frequency 2-D polynomial model was used, $\Gamma(\boldsymbol{\rho}, f, t) = \mathbf{Y}_1 + \mathbf{Y}_2 f + \mathbf{Y}_3 t$ and $\Psi(\boldsymbol{\rho}, f, t) = \mathbf{T}_1 + \mathbf{T}_2 f + \mathbf{T}_3 t$, with randomly selected “true” polynomial coefficient matrices \mathbf{Y}_d and \mathbf{T}_d . The same 10 calibrator sources and beam steering direction as in the previous section were used in this simulation. CRB values were computed using (18), now with the frequency-time constraint Jacobian $\mathbf{F}_{k,m}$ from (26).

Fig. 5 presents CRB results for four linear in frequency gain and phase coefficients, i.e., entries of \mathbf{Y}_2 and \mathbf{T}_2 corresponding to source 3 and core station 2 and the respective source 3 entries from outer station 35. An important feature is that the CRBs are unacceptably high unless the estimation domain covers several seconds and/or a few hundred kilohertz. This is because sufficient frequency-time diversity due to fringe rotation in $\mathbf{K}_{k,m}$ is needed to overcome the multiple source ambiguity discussed in Section III-A.

The scenario of Fig. 5 was repeated for Fig. 6 with the following changes: 1) the central core direction independent model was applied, by combining (23) and (26); 2) the scene contained

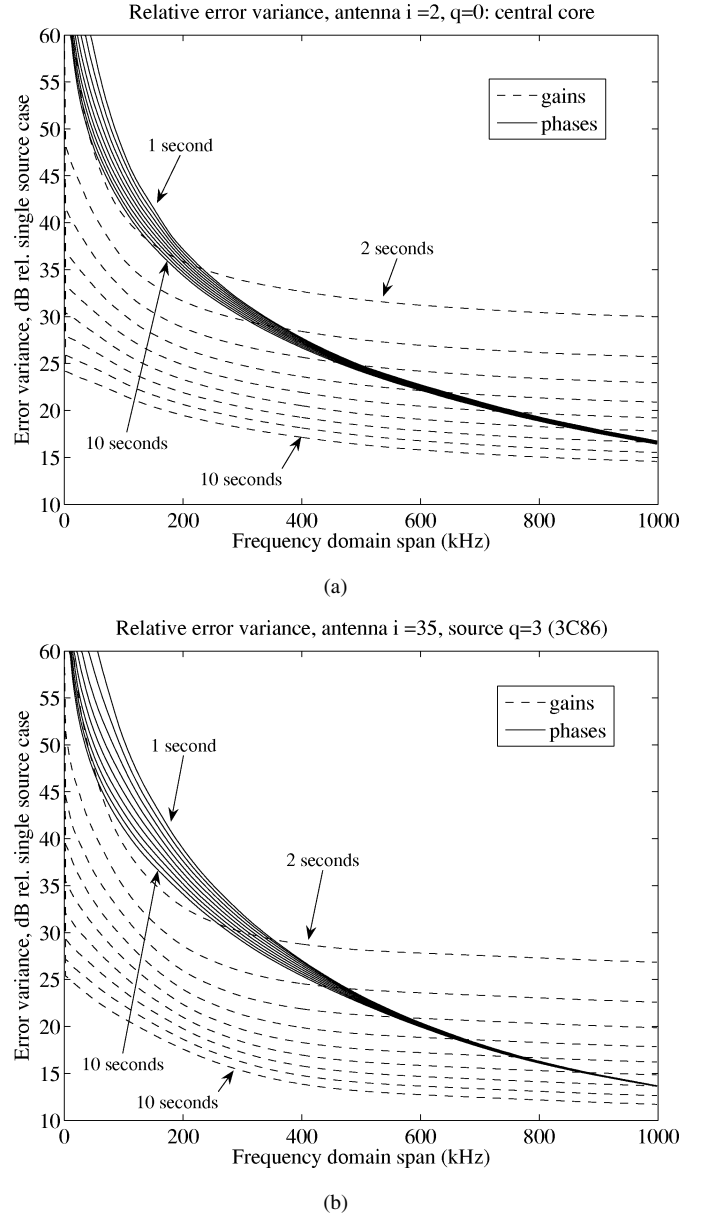


Fig. 5. Normalized CRB for polynomial coefficients as a function of total frequency-time span. The direction independent compact core model was *not* used. Decibel level is normalized to the single source CRB over the same frequency-time span. STI sample spacing is 1.0 s by 2.0 kHz, beginning at 40 MHz. (a) Normalized CRB for the gain, $(\mathbf{Y}_2)[2, 3]$, and phase, $(\mathbf{T}_2)[2, 3]$, coefficients from the linear-in-frequency polynomial term for station 2 (in the central core) and source $q = 3$. Curve families cover CRB dependence on time domain size from 1 to 10 s in 1 second increments. The 1-s gain curve is off the plot scale above. (b) CRB for $(\mathbf{Y}_2)[35, 3]$ and $(\mathbf{T}_2)[35, 3]$, at station 35 in an outer array arm.

only the first five sources from Table I; and 3) the 2-D frequency-time polynomial was first order in frequency, and zero order in time: $\Gamma(\boldsymbol{\rho}, f, t) = \mathbf{Y}_1 + \mathbf{Y}_2 f$, $\Psi(\boldsymbol{\rho}, f, t) = \mathbf{T}_1 + \mathbf{T}_2 f$. This scenario will be used without change in all following experiments to exploit the central core and to reduce computational burden in simulations which involve many Monte Carlo random trials.

Comparing Figs. 6 and 5(a) it is apparent that the central core model significantly reduces estimation error variance and the need for large time domain span. Other experiments (not shown)

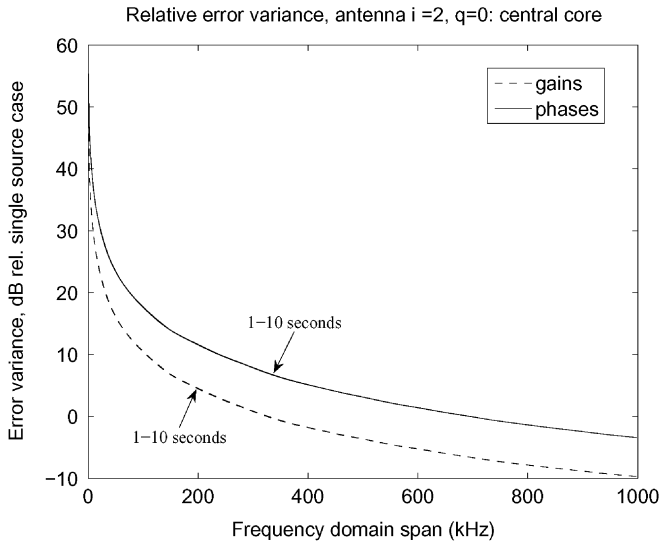


Fig. 6. Normalized CRB for linear in frequency coefficients $(\mathbf{Y}_2)[2, 0]$, gain, and $(\mathbf{T}_2)[2, 0]$, phase, when using the direction independent compact core model, corresponding to station 2 and “source” $q = 0$ in the indexing scheme of (22). Note that when using the compact core direction independent model, error variance on time domain span is minimal.

indicate that the reduction from 10 to five sources and use of a zero-order-in-time polynomial model were minor factors in this CRB reduction. This suggests that a self-calibration algorithm should exploit the central core model if array geometry and ionospheric structure support it.

C. Peeling Calibration Performance

A full implementation of the peeling algorithm was run using synthesized array receiver data to compare its performance with the corresponding CRB. When fully operational, LOFAR will be calibrated in real time using a super computer. However, given existing computational resources and the need to run many Monte Carlo trials, the thinned array five-source scenario of Fig. 6 was used here.

A first order in frequency, zero order in time, 2-D polynomial was applied both for generating the simulated array data, $\mathbf{x}_k(n)$, and in the peeling algorithm parameter model. The “true” parameter matrices were randomly generated. The frequency-time STI bin size is 2 kHz by 1 s, with $K_b = 50$, $M_b = 10$. The Peeling block size is 100 kHz by 10 s, and with $1 \leq \tilde{k} \leq 10$, $\tilde{m} = 1$, the total domain covers 40.0 to 41.0 MHz and 10 s. Peeling used $I = 5$ iterations.

The generated array data had a central core ($J_c = 16$), and the CRB analysis takes this into account. Thus the CRB evaluation uses the product of (23) and (26) as the constraint Jacobian, $\mathbf{F}_{k,m}$. However, the current version of Peeling does not include specific provision to exploit the central core model, so it generates distinct calibrations for each source-station combination, even though they should be direction-independent and thus identical for all sources for each central core station. As final estimate for the core array calibration parameters, only the parameters derived from the brightest ($q = 1$) source are used.

Fig. 7 shows the CRB and Peeling estimation error sample variance averaged over 100 Monte Carlo trials. It is seen that

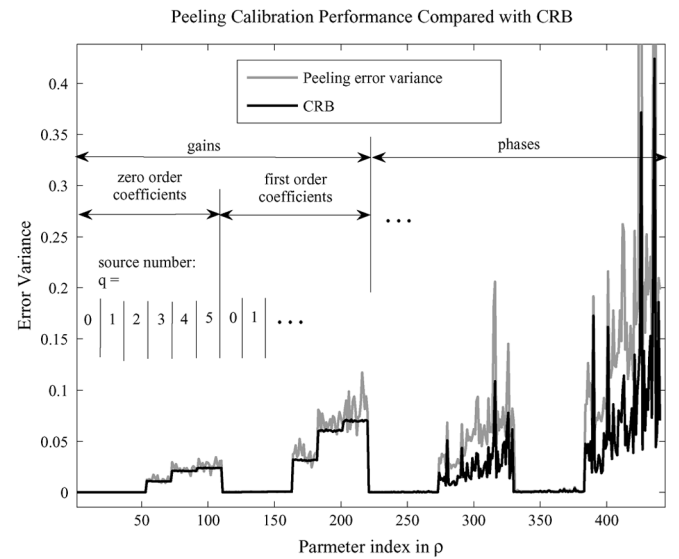


Fig. 7. Peeling algorithm performance comparison with the CRB. Estimation domain size is 10 s by 1.0 MHz, with 1 s by 2 kHz STI sample spacing. Source index $q = 0$ represents the central core subarray, whose calibration polynomial coefficients do not depend on source direction. The horizontal axis parameter index for elements of \mathbf{p} is ordered as in (25).

Peeling closely approaches the CRB performance bound for the central core array ($q = 0$) and the two brightest sources ($q = 1, 2$). Peeling error variance is somewhat higher than the CRB for the three weaker sources ($q = 3, 4, 5$). This suggests that there is value in continued research to develop improved calibration algorithms. The plotted results are encouraging, but need to be verified on the full array and with a larger number of sources.

D. Peeling With Demixing

Performance of the combined Peeling with Demixing procedure was evaluated by computer simulation with the same models and parameter settings as used in Fig. 6 and Section IV-C. Fig. 8 compares the average bias error magnitude for single pass conventional Peeling with the bias from Peeling with Demixing. Estimation error variance (not shown) was acceptably low and at the same level with and without demixing. The figure shows that demixing significantly reduced bias error.

Without demixing, Peeling requires $I = 3$ passes to produce bias levels comparable to one pass of Demixed Peeling. This demonstrates the theoretical correctness of the approach described in Section III-E. However, its practical utility is somewhat questionable: With our current implementation in Matlab it takes 3.31 times as long to complete a single demix pass as to complete three passes of the regular peeling algorithm. Since both performance and complexity depend on the number of sources Q and other system parameters and assumptions, it is hard to predict how this works out in the actual LOFAR system.

V. CONCLUSION

Calibration algorithm development for LOFAR is ongoing and is critically important if the system is to achieve its ambitious scientific goals of observing the very weak signals generated during the early evolution of the universe. Interaction

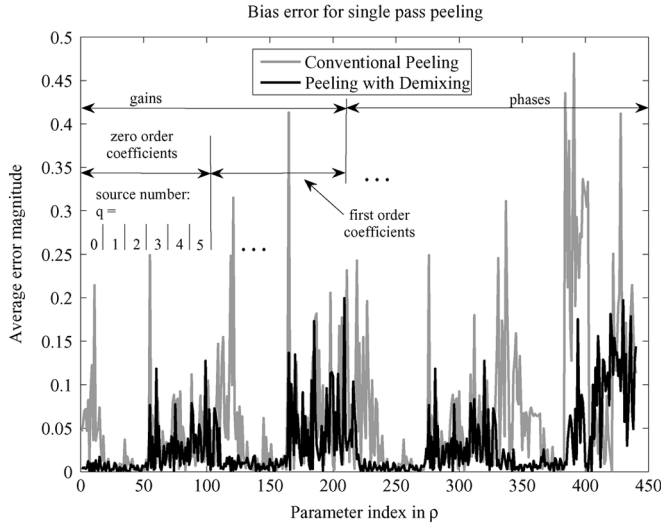


Fig. 8. Comparison of bias error in estimating polynomial parameter ρ_q , $0 \leq q \leq 5$ for Peeling alone, and Peeling with Demixing. One peeling pass was performed in each case. The plot illustrates the lower bias error performance of the demixing algorithm. Without demixing (not shown in this plot) three to four passes of Peeling were needed to achieve the bias levels of the lower curve. Ten Monte Carlo trials were used to compute average error magnitude. In all other details the algorithm and source parameters were identical to those used in Fig. 7.

with the ionosphere at low frequencies makes this self-calibration problem significantly different and more difficult than what has been encountered in existing radio synthesis imaging instruments. It also leads to new challenges in array signal processing.

The main point of the paper was to derive and present the machinery for answering fundamental questions about calibratability for LOFAR, and in particular to assess the previously open issue of whether it is even theoretically possible to achieve self-calibration. The most significant finding is that without making assumptions on the ionospheric structure, LOFAR cannot be calibrated, but with some modeling assumptions (e.g., frequency-time polynomial smoothing) and sufficient frequency-time diversity from large estimation domains, direction dependent calibration is possible. CRB analysis revealed no “show stopping” theoretical limitations on the ability to calibrate LOFAR. A central core configuration gives a significant reduction in the number of unknown parameters and thus greatly enhances the calibration performance.

The Peeling calibration algorithm was implemented and compared to the CRB using simulated data. The results indicate that at least for the limited scenarios evaluated, Peeling appears to be a viable candidate. Further algorithm development to reduce computational complexity and estimation bias due to multiple sources is warranted. Next steps will also include algorithm development to directly exploit the central core direction independent calibration model in Peeling, study of new methods to achieve more effectively reduced cross-source interference bias at the start of Peeling, and evaluation of ionospheric data and physical models to determine appropriate smoothing functions over time, frequency and space with a reduced number of parameters. To complete the picture, further studies also need to point out: i) the accuracy of these models (model mismatch, which translates into bias) and ii) the consequences of parameter variance on the dynamic range of the image.

APPENDIX

Here, we derive the closed form expressions for $\mathbf{M}_{k,m}$ in (8) which are shown in (9)–(14). Subscripts k and m are dropped for notational simplicity.

Define the Jacobians

$$\begin{aligned} \mathbf{J}_{\gamma_q} &= \frac{\partial \text{vec}(\mathbf{R})}{\partial \gamma_q^T}, & \mathbf{J}_{\psi_q} &= \frac{\partial \text{vec}(\mathbf{R})}{\partial \psi_q^T} \\ \mathbf{J}_{\lambda} &= \frac{\partial \text{vec}(\mathbf{R})}{\partial \lambda^T}. \end{aligned}$$

The following expressions are useful in computing the partial derivatives:

$$\begin{aligned} \text{vec}(\mathbf{R}) &= \sum_{q=1}^Q \sigma_q^2 (\bar{\mathbf{a}}_q \otimes \mathbf{a}_q) + \text{vec}(\Lambda) \\ \frac{\partial \mathbf{a}_q}{\partial \gamma_q^T} &= \Phi_q, & \frac{\partial \mathbf{a}_q}{\partial \phi_q^T} &= j\mathbf{E}_q \end{aligned}$$

where $\mathbf{E}_q = \text{diag}(\gamma_q \odot \mathbf{k}_q)$ and $\Phi_q = \text{diag}(\phi_q \odot \mathbf{k}_q)$. The Jacobians can then be evaluated as

$$\begin{aligned} \mathbf{J}_{\gamma_q} &= \frac{\partial}{\partial \gamma_q^T} \left(\sum_{p=1}^Q \sigma_p^2 (\bar{\mathbf{a}}_p \otimes \mathbf{a}_p) + \text{vec}(\Lambda) \right) \\ &= \sigma_q^2 \frac{\partial \bar{\mathbf{a}}_q}{\partial \gamma_q^T} \otimes \mathbf{a}_q + \sigma_q^2 \bar{\mathbf{a}}_q \otimes \frac{\partial \mathbf{a}_q}{\partial \gamma_q^T} \\ &= \sigma_q^2 \Phi_q \otimes \mathbf{a}_q + \sigma_q^2 \bar{\mathbf{a}}_q \otimes \Phi_q \\ \mathbf{J}_{\psi_q} &= \frac{\partial}{\partial \psi_q^T} \left(\sum_{p=1}^Q \sigma_p^2 (\bar{\mathbf{a}}_p \otimes \mathbf{a}_p) + \text{vec}(\Lambda) \right) \\ &= \sigma_q^2 \frac{\partial \bar{\mathbf{a}}_q}{\partial \psi_q^T} \otimes \mathbf{a}_q + \sigma_q^2 \bar{\mathbf{a}}_q \otimes \frac{\partial \mathbf{a}_q}{\partial \psi_q^T} \\ &= -j\sigma_q^2 \bar{\mathbf{E}}_q \otimes \mathbf{a}_q + \sigma_q^2 \bar{\mathbf{a}}_q \otimes j\mathbf{E}_q \\ \mathbf{J}_{\lambda} &= \frac{\partial \text{vec}(\Lambda)}{\partial \lambda^T} = \mathbf{I} \circ \mathbf{I}. \end{aligned}$$

An expression is derived here for $\mathbf{M}_{\gamma_p \psi_q}$ as given in (15), the other blocks are derived similarly.

$$\begin{aligned} \mathbf{M}_{\gamma_p \psi_q} &= \mathbf{J}_{\gamma_p}^H (\bar{\mathbf{R}}^{-1} \otimes \mathbf{R}^{-1}) \mathbf{J}_{\psi_q} \\ &= (\Phi_p \otimes \mathbf{a}_p^H + \mathbf{a}_p^T \otimes \Phi_p^H) (\bar{\mathbf{R}}^{-1} \otimes \mathbf{R}^{-1}) \\ &\quad \times (-j\bar{\Phi}_q \otimes \mathbf{a}_q + \bar{\mathbf{a}}_q \otimes -j\Phi_q) \\ &= \sigma_p^2 \sigma_q^2 \left(-j(\Phi_p^T \bar{\mathbf{R}}^{-1} \bar{\mathbf{E}}_q) \otimes (\mathbf{a}_p^H \mathbf{R}^{-1} \mathbf{a}_q) \right. \\ &\quad \left. + j(\Phi_p^T \bar{\mathbf{R}}^{-1} \bar{\mathbf{a}}_q) \otimes (\mathbf{a}_p^H \mathbf{R}^{-1} \mathbf{E}_q) \right. \\ &\quad \left. - j(\mathbf{a}_p^T \otimes \bar{\mathbf{R}}^{-1} \bar{\mathbf{E}}_q) \otimes (\Phi_p^H \mathbf{R}^{-1} \mathbf{a}_q) \right. \\ &\quad \left. + j(\mathbf{a}_p^T \bar{\mathbf{R}}^{-1} \bar{\mathbf{a}}_q) \otimes (\Phi_p^H \mathbf{R}^{-1} \mathbf{E}_q) \right) \\ &= 2\sigma_p^2 \sigma_q^2 \text{Im} \left\{ (\Phi_p^T \bar{\mathbf{R}}^{-1} \bar{\mathbf{E}}_q) (\mathbf{a}_p^H \mathbf{R}^{-1} \mathbf{a}_q) \right. \\ &\quad \left. + (\Phi_p^T \bar{\mathbf{R}}^{-1} \bar{\mathbf{a}}_q) (\mathbf{a}_p^H \mathbf{R}^{-1} \mathbf{E}_q) \right\}. \end{aligned}$$

ACKNOWLEDGMENT

The authors acknowledge the invaluable help received from J. Noordam, A.-J. Boonstra, R. Nijboer, and S. Wijnholds, all of ASTRON, The Netherlands. Their input in defining the problem and describing the operation of LOFAR was critical in enabling this work.

REFERENCES

- [1] S. van der Tol, B. Jeffs, and A. J. van der Veen, "Calibration of a large distributed low frequency radio astronomical array (LOFAR)," in *EU-SIPCO*, Antalya (T), Sep. 2005, EURASIP.
- [2] B. Jeffs, S. van der Tol, and A. J. van der Veen, "Direction dependent self-calibration of large distributed sensor arrays," in *Proc. IEEE ICASSP*, Toulouse, France, May 2006, vol. IV, pp. 1069–1072.
- [3] A. R. Thompson, J. M. Moran, and G. W. Swenson Jr., *Interferometry and Synthesis in Radio Astronomy*, 2nd ed. New York: Wiley-Interscience, 2001.
- [4] R. A. Perley, F. R. Schwab, and A. H. Bridle, Eds., *Synthesis Imaging in Radio Astronomy, A collection of Lectures from the Third NRAO Synthesis Imaging Summer School*. San Francisco, CA: Astronom. Soc. Pacific, 1989, vol. 6.
- [5] G. B. Taylor, C. L. Carilli, and R. A. Perley, Eds., *Synthesis Imaging in Radio Astronomy II: A Collection of Lectures From the Sixth NRAO/NMIMT Synthesis Imaging Summer School*. San Francisco, CA: Astronom. Soc. Pacific, 1999.
- [6] A. J. van der Veen, A. Leshem, and A. J. Boonstra, P. J. Hall, Ed., "Array signal processing for radio astronomy," in *The Square Kilometre Array: An Engineering Perspective*. Dordrecht, Germany: Springer, 2005, pp. 231–249, ISBN 1-4020-3797-x. Reprinted from *Experimental Astronomy*, 17(1–3), 2004.
- [7] S. J. Wijnholds and A. J. Boonstra, "A multisource calibration method for phased array radio telescopes," in *IEEE Wkshp. Sensor Array and Multichannel*, Boston, MA, Jul. 2006, pp. 200–204.
- [8] C. Lonsdale, "Calibration Approaches MIT Haystack, Tech. Rep. MIT Low Frequency Program, Memo #015, Aug. 2003 [Online]. Available: <http://www.haystack.mit.edu/ast/arrays/mwa/LFD/documents.html>
- [9] A.-J. Boonstra and A.-J. van der Veen, "Gain calibration methods for radio telescope arrays," *IEEE Trans. Signal Process.*, vol. 51, no. 1, pp. 25–38, Jan. 2003.
- [10] J. E. Noordam, "LOFAR calibration challenges," in *Proc. SPIE*, Oct. 2004, vol. 5489, pp. 817–825.
- [11] T. J. Cornwell and P. N. Wilkinson, "A new method for making maps with unstable radio interferometers," *Mon. Not. R. Astron. Soc.*, vol. 196, pp. 1067–1086, 1981.
- [12] J. E. Noordam and A. G. de Bruyn, "High dynamic range mapping of radio sources, with application to 3C84," *Nature*, vol. 299, pp. 597–600, 1982.
- [13] T. J. Pearson and A. C. S. Readhead, "Image formation by self-calibration in radio astronomy," *Ann. Rev. Astron. Astrophys.*, vol. 22, pp. 97–130, 1984.
- [14] M. H. Wieringa, "An investigation of the telescope based calibration methods 'redundancy' and 'self-cal'," *Experiment. Astron.*, vol. 2, pp. 203–225, 1992.
- [15] J. A. Högbom, "Aperture synthesis with a nonregular distribution of interferometer baselines," *Astron. Astrophys. Suppl.*, vol. 15, pp. 417–426, 1974.
- [16] U. J. Schwarz, "Mathematical-statistical description of the iterative beam removing technique (method CLEAN)," *Astron. Astrophys.*, vol. 65, pp. 345–356, 1978.
- [17] J. E. Noordam, "Generalized self-calibration for LOFAR," in *URSI General Assembly*, Maastricht, The Netherlands, Aug. 2002 [Online]. Available: <http://www.ursi.org/Proceedings/ProcGA02/papers/1087.pdf>
- [18] B. Friedlander and A. J. Weiss, "Direction finding in the presence of mutual coupling," *IEEE Trans. Antennas Propag.*, vol. 39, pp. 273–284, Mar. 1991.
- [19] B. C. Ng and C. M. S. See, "Sensor-array calibration using a maximum-likelihood approach," *IEEE Trans. Antennas Propag.*, vol. 44, pp. 827–835, June 1996.
- [20] A. Flieller, A. Ferreol, P. Larzabal, and H. Clergeot, "Robust bearing estimation in the presence of direction-dependent modelling errors: Identifiability and treatment," *IEEE ICASSP*, pp. 1884–1887, Apr. 1995.
- [21] G. C. Brown, J. H. McClellan, and E. J. Holder, "A homotopy continuation approach for self-calibration of arrays with general phase perturbations," in *IEEE Sixth SP Wkshp. Stat. Signal Array Process.*, Oct. 1992, pp. 263–266.
- [22] A. J. Weiss and B. Friedlander, "Array processing using joint diagonalization," *Signal Process.*, vol. 50, pp. 205–222, May 1996.
- [23] D. R. Fuhrmann, "Estimation of sensor gain and phase," *IEEE Trans. Signal Process.*, vol. 42, pp. 77–87, Jan. 1994.
- [24] M. Pesavento, A. B. Gershman, and K. M. Wong, "Direction finding in partly calibrated sensor arrays composed of multiple subarrays," in *IEEE Trans. Signal Process.*, Sept. 2002, vol. 50, pp. 2103–2115.
- [25] C.M.S. See and A. B. Gershman, "Direction-of-arrival estimation in partly calibrated subarray-based sensor arrays," in *IEEE Trans. Signal Process.*, Feb. 2004, vol. 52, pp. 329–338.
- [26] J. P. Hamaker, J. D. Bregman, and R. J. Sault, "Understanding radio polarimetry. I. Mathematical foundations," *Astron. Astrophys. Suppl. Ser.*, vol. 117, pp. 137–147, May 1996.
- [27] J. E. Noordam, "The measurement equation of a generic radio telescope, AIPS++ implementation note nr 185 Tech. rep., ASTRON, 1996.
- [28] S. M. Kay, *Fundamentals of Statistical Signal Processing: Estimation Theory*. Englewood Cliffs, NJ: Prentice-Hall, 1993.
- [29] S. J. Wijnholds, J. D. Bregman, and A. J. Boonstra, "Sky noise limited snapshot imaging in the presence of RFI with LOFAR's initial test station," *Exper. Astron.*, vol. 17, pp. 35–42, Jun. 2004.
- [30] A. S. Bennett, "The revised 3C catalog of radio sources," *Memoires Royal Astron. Soc.*, vol. 68, pp. 163–172, 1962.



Sebastiaan van der Tol (S'05) was born in The Netherlands in 1977. He received the M.Sc. degree in electrical engineering from Delft University of Technology, The Netherlands, in 2004.

Since January 2004, he has been a Research Assistant with the same institute, where he is pursuing the Ph.D. degree in electrical engineering. His current research interests include array signal processing and interference mitigation techniques for large phased array radio telescopes.



Brian D. Jeffs (M'90–SM'02) received the B.S. and M.S. degrees in electrical engineering from Brigham Young University, Provo, UT, in 1978 and 1982, respectively. He received the Ph.D. degree from the University of Southern California, Los Angeles, in 1989, also in electrical engineering.

He is currently an Associate Professor with the Department of Electrical and Computer Engineering at Brigham Young University, where he lectures in the areas of digital signal processing, digital image processing, and probability theory. Current research interests include array signal processing for radio astronomy, RF interference mitigation, MIMO wireless communications, and digital image restoration. Previously, he was with the Hughes Aircraft Company where he served as a Sonar Signal Processing Systems Engineer in the Antisubmarine Warfare Group. Responsibilities there included algorithm development and system design for digital sonars in torpedo, surface ship towed array, and helicopter dipping array platforms.

Dr. Jeffs was a Vice General Chair for the IEEE ICASSP-2001, held in Salt Lake City, UT. He was a member of the executive organizing committee for the 1998 IEEE DSP Workshop, and served several years as chair of the Utah Chapter of the IEEE Communications and Signal Processing Societies.



Alle-Jan van der Veen (M'95–SM'03–F'05) was born in The Netherlands in 1966. He received the Ph.D. degree (*cum laude*) from Delft University of Technology (TU), Delft, The Netherlands, in 1993.

Throughout 1994, he was a Postdoctoral Scholar with Stanford University, Stanford, CA. At present, he is a Full Professor of signal processing at TU Delft. His research interests are in the general area of system theory applied to signal processing, and in particular, algebraic methods for array signal processing, with applications to wireless communications and radio

astronomy.

Dr. van der Veen is the recipient of a 1994 and 1997 IEEE Signal Processing Society (SPS) Young Author paper award, and was an Associate Editor for the IEEE TRANSACTIONS ON SIGNAL PROCESSING (1998–2001), Chairman of the IEEE SPS Signal Processing for Communications Technical Committee (2002–2004), and Editor-in-Chief of the IEEE SIGNAL PROCESSING LETTERS (2002–2005). He is currently Editor-in-Chief of the IEEE TRANSACTIONS ON SIGNAL PROCESSING, and member-at-large of the Board of Governors of IEEE SPS.